

A plasticity constitutive model for concrete under multiaxial compression

B.T. Zheng^a and J.G. Teng^{a*}

^aDepartment of Civil and Environmental Engineering, The Hong Kong Polytechnic University, Hong Kong SAR, China. E-mail (Bo-Tong Zheng): btzheng@polyu.edu.hk

*Corresponding author, E-mail: cejgteng@polyu.edu.hk

Abstract

Structural members with confined concrete are becoming increasingly popular in civil engineering applications because of their superior strength and ductility. In these structural members, the concrete is subjected to dilation-induced (passive) lateral compressive stresses from the confining device (e.g., a steel tube). Existing research has led to theoretical models that predict closely the stress-strain behavior of concrete under uniform confinement (e.g., concrete in circular steel tubes under concentric axial compression), but theoretical models with a similar capability have not been achieved for the more common situation of concrete under non-uniform confinement (e.g., concrete in rectangular steel tubes). This paper presents a three-dimensional (3D) plasticity constitutive model that is accurate in predicting the stress-strain behavior of concrete in various scenarios of confinement. In the proposed model, a well-established open strength surface with associated open yield surfaces is combined with a hardening/softening rule compatible with both plastic volumetric compaction and dilation. In addition, a novel potential surface with a triangle-like deviatoric trace is proposed and calibrated with available experimental data of non-uniformly confined concrete. The implementation of the constitutive model in finite element analysis with an enhanced stress-return algorithm suitable for the novel

potential surface is explained. While the focus of the present work is on monotonic compression-dominated loading, the model can be combined with fracture and damage theories to depict the behavior of concrete under tension-dominated and cyclic loading conditions. The performance of the proposed model is evaluated by comparing its predictions with a wide range of experimental data covering uniform active, uniform passive, and non-uniform passive confinement conditions, which demonstrates the capability and high accuracy of the proposed model.

Keywords: Concrete, Multiaxial compression, Confined concrete, Plasticity model, Constitutive model

1. Introduction

Concrete is commonly employed in structural members to resist axial compression and is often laterally confined to enhance its strength and deformation capacity. In such structural members, the axial compression on the concrete induces lateral dilation, which is then resisted by the confining device (e.g., a steel tube), leading to lateral compressive stresses (i.e., confining stresses) on the concrete. In turn, the confining stresses influence the strength and deformation behavior of the concrete. Therefore, the mechanical behavior of confined concrete in structural members involves an intricate relationship between the multiaxial stress-strain behavior of concrete and the dilation-confinement interaction between the concrete and the confining device. To be able to closely predict the behavior of such structural members, an accurate stress-strain (i.e.,

constitutive) model for the confined concrete, which is typically under multiaxial compression, is a pre-requisite.

The multiaxial strength behavior of concrete has been well-established through extensive experimental and theoretical research (e.g., [1–4]). However, the dilation-confinement interaction of confined concrete is dependent on both the dilation behavior of the concrete itself and the material and form of the confining device. The available confining materials have evolved over the years: from the predominant use of mild steel (e.g., [5,6]) to the increasing use of high-strength steel (HSS) (e.g., [7,8]) and fiber-reinforced polymer (FRP) composites (e.g., [9,10]). Meanwhile, the confinement form has also evolved to maximize the benefit of confinement through layout optimization of the confining device and the synergistic combination of different confining materials. As a result, an accurate prediction of the mechanical behavior of confined concrete is generally a considerable challenge in the modeling of confined-concrete members of various forms.

The typical tensile stress-strain curves of three commonly used confining materials are presented in Fig. 1a, together with the stress-strain curves of concrete uniformly confined with these three materials (Fig. 1b). For the purpose of discussion, the three confining devices examined in Fig. 1b were assumed to have the same confinement stiffness and no axial resistance (e.g., steel tubes without axial interaction with the concrete and FRP tubes with fibers oriented in the hoop direction). Mild steel exhibits a relatively short linear elastic stage, followed by a yield plateau (Fig. 1a). If the confinement is uniform (more precisely, circumferentially uniform, with the axial distributions of confining stresses being uniform or approximated as being uniform as has been

commonly done in existing studies) (Fig. 2a), such as that in a concentrically loaded concrete column confined with a steel tube, the confining stress of mild steel-confined concrete is little affected by dilation once the yield plateau is reached. Therefore, the behavior of such mild steel-confined concrete is similar to that of concrete subjected to an externally imposed, constant confining stress (referred to as active confinement), in which the dilation-confinement interaction does not exist. Accordingly, purely one-dimensional algebraic axial stress-strain models for direct prediction of axial stress-strain curves (e.g., without explicit consideration of lateral strains or dilation-confinement interactions), referred to as direct analytical models, have been developed for concrete confined by mild steel (e.g., [11]) based on investigations on actively-confined concrete.

By contrast, FRP is linear elastic up to tensile rupture, so the confining stress in FRP-confined concrete is a reaction to and thus dependent on dilation, and this type of confinement is referred to as passive confinement. For passively-confined concrete, active-confinement models, which do not capture the dilation-confinement interaction in passive-confined concrete, are no longer suitable. By implicitly incorporating the dilation behavior of concrete, many direct analytical models, often referred to as design-oriented models [12], have been developed for concrete under uniform passive confinement offered by FRP (e.g., [13,14]). While such models are acceptably accurate for FRP-confined concrete, they cannot accurately describe the stress-strain behavior of concrete confined with other materials such as mild steel or HSS, as the dilation-confinement interaction with FRP is implicitly accounted for in these models.

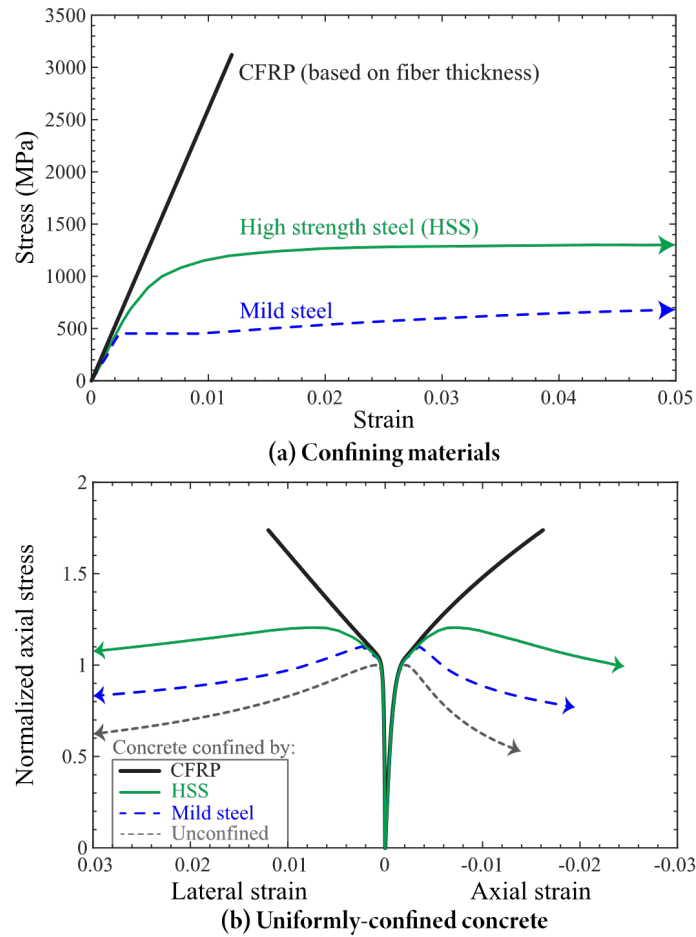


Fig.1 Stress-strain curves of confining materials and corresponding uniformly-confined concrete

More sophisticated models that account explicitly for the dilation-confinement interaction through an incremental procedure have also been developed for concrete subjected to passive uniform confinement, and these models are commonly referred to as analysis-oriented models [12]. It should be noted that ‘volumetric dilation’ is generally used in the present paper to include positive, zero or negative volumetric changes (i.e., “volumetric expansion”, “volumetric conservation”, or “volumetric compaction” respectively), but it means only “volumetric expansion” when used in contrast with “volumetric compaction”. In an analysis-oriented model,

the volumetric dilation behavior of concrete is typically defined using an axial strain-lateral strain relationship considering the confining stress level (e.g., [15–17]), based on the experimental data of concrete under both uniform active confinement (e.g., [1,18]) and uniform passive confinement (e.g., [12,19,20]). Therefore, these analysis-oriented models are suitable for concrete confined with different confining materials, and the stress-strain curve of concrete confined with a specific confining material can be properly captured through an incremental analysis process. As an illustration, the stress-strain curves of concrete confined with mild steel, FRP, and HSS, respectively, as predicted using the model of Jiang and Teng [16], are given in Fig. 1b, where the three confining devices have the same confinement stiffness and no axial resistance. These predicted curves exhibit the distinctive behaviors of concrete with mild steel and FRP as confining materials and also reveal the transition of HSS-confined concrete from an initial bi-linear response, typical of passive-confinement by a linear-elastic device, to a gradually softening axial stress-strain response as dictated by the stress-strain curve of HSS (i.e., a wide strain range of linear elasticity followed by a strain-hardening yielding stage that gradually levels out).

The analysis-oriented models described in the above paragraph were developed for concrete subjected to uniform confinement, and are thus not normally suitable for or extendable to concrete subjected to non-uniform confinement. The volumetric dilation model in such an analysis-oriented model is essentially two dimensional (2D), with the relationship between the confining stress and the lateral strain being only one-dimensional (1D). Using the compression-negative notation, the principal stress relationship of $\sigma_1 \geq \sigma_2 > \sigma_3$ holds for concrete under non-uniform confinement, where σ_3 is the dominant axial compressive stress while σ_1 and σ_2 are the principal lateral confining stresses. For uniformly-confined concrete, as shown in Fig. 2a, $\sigma_1 = \sigma_2 = \sigma_l$

everywhere in the concrete, where σ_l is the lateral confining stress; and the resulting lateral principal strains (dilations) are also equal (Fig. 2d), that is $\varepsilon_1 = \varepsilon_2 = \varepsilon_l$, where ε_l is the lateral strain. Therefore, the 2D volumetric dilation model is suitable only for uniform confinement. For concrete under non-uniform confinement, as illustrated via the examples shown in Figs. 2b and c for typical non-circular-section members, the principal confining stresses are different (i.e., $\sigma_1 > \sigma_2$) and the resulting lateral strains unequal (i.e., $\varepsilon_1 > \varepsilon_2$) (see Fig. 2e) except at the center of a square section.

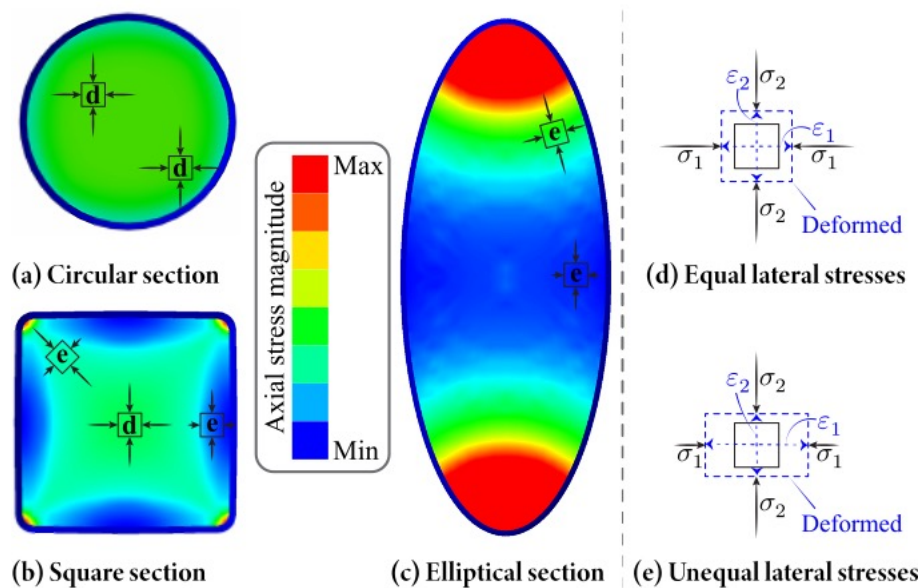


Fig.2 Stress states in confined-concrete members under compression

Consequently, the 2D volumetric dilation model is insufficient and unsuitable for non-uniformly confined concrete. Indeed, non-uniform confinement is predominant in practice due to the inevitable eccentricity of axial compression (e.g., [21]), wide use of non-circular cross-sections (e.g., [22]), and synergistic combination of multiple confining devices/materials (e.g., [23,24]). Therefore, a three-dimensional (3D) constitutive model is necessary to incorporate an additional

dimension for the deviatoric behavior to accommodate the difference between ε_1 and ε_2 corresponding to the unequal principal confining stresses σ_1 and σ_2 .

Plasticity-based constitutive models depicting the full 3D incremental stress-strain relationship are capable of depicting both the strength and deformation characteristics of confined concrete simultaneously. However, most of the existing concrete plasticity models have been developed mainly for concrete under multiaxial stresses due to imposed loading inducing active stresses [25–30], without adequate attention to the response of concrete under non-uniform passive confinement, where typically the concrete has been severely damaged/cracked but remains apparently intact or even hardened due solely to passive confinement. Being typical phenomenological models, plasticity-based constitutive models are highly dependent on experimental observations against which they are developed and calibrated. Therefore, the existing models, in general, are inadequate for predicting the mechanical behavior of confined concrete subjected to passive, non-uniform confinement. Nevertheless, since the multiaxial strength behavior of concrete is nearly path-independent [1], the components of these models regarding the strength behavior are generally appropriate for passively-confined concrete. Therefore, it is the components pertaining to the dilation behavior of concrete that need to be improved to properly capture the deformation characteristics of concrete subjected to passive, non-uniform confinement.

The deformation behavior of concrete can be split into two components: volumetric dilation behavior and deviatoric dilation behavior. The former depends on the ratio between the axial principal strain and the sum of the lateral principal strains, while the latter depends on the ratio

between the two lateral principal strains; their mathematical definitions are given later in the paper. For the volumetric dilation behavior of passively-confined concrete, plasticity models with a Drucker-Prager (D-P) flow rule have been developed based on the experimental data of FRP-confined concrete [10,31–34]. All these models have limitations in describing the volumetric dilation behavior of passively-confined concrete as critically reviewed in Yu et al. [34]. Accordingly, since the analysis-oriented model of Teng et al. [15] is highly accurate for both uniform active confinement and uniform passive confinement, a process was developed to combine the model of Teng et al. [15] with the built-in D-P plasticity model [34] in ABAQUS [35]. The resulting analytically augmented (AA) plasticity model can closely predict the behavior of concrete under both uniform active confinement and uniform passive confinement, and it has since been widely adopted and investigated in subsequent studies (e.g., [36,37]). However, since the core relationship relating the confining stress to the lateral strain is a 1D equation, this model is inaccurate for concrete under non-uniform confinement.

An approximate method was proposed by Yu et al. [38] to deal with this limitation by converting the two unequal principal confining stresses σ_1 and σ_2 in non-uniformly confined concrete into one equivalent confining stress σ_l . While σ_l can be input into the analytical relationship of Teng et al. [15] to predict the volumetric dilation behavior, the deviatoric dilation behavior still cannot be specified and is therefore automatically dealt with by the built-in plasticity-based model with a D-P type plastic potential surface, which is characterized by hyperbolic meridians and circular deviatoric traces (for more details, see sub-sections 2.2 and 2.3). That is, the lateral principal strains ε_1 and ε_2 corresponding to σ_1 and σ_2 are simply predicted by the D-P type plasticity model's deviatoric component. While the obtained equivalent lateral strain ε_l is approximate, the

dominant inaccuracy arises from the prediction of ε_1 and ε_2 through the built-in model. This inaccuracy is clearly seen in the predictions of the compression tests of concrete under non-uniform passive confinement using this AA plasticity-based model [37,39], where the prediction of ε_l was calibrated with the experimental dilation data [40], but the predictions of ε_1 and ε_2 still deviated much from the experimental data. The reason is that the deviatoric component of the D-P type potential surface is inadequate in predicting the deviatoric dilation for non-uniformly confined concrete. Nonetheless, this AA plasticity-based model is accurate for uniformly confined concrete while often providing a reasonable treatment for non-uniformly-confined concrete; it has therefore been widely used in subsequent studies (e.g., [41–43]). Other plasticity models developed by considering the volumetric behavior of both actively- and passively-confined concrete (e.g., [44–47]) have the same limitation that the deviatoric component is unsuitable for non-uniformly confined concrete. Therefore, a 3D plasticity constitutive model capable of accurate prediction of the deviatoric dilation behavior of non-uniformly confined concrete is required for the accurate modeling of structural members with confined concrete.

Moreover, such a 3D plasticity-based constitutive model must be implemented into a 3D finite element (FE) model to conduct non-linear analysis of structural members with dilation-confinement interaction. In structural members such as a concrete-filled steel tube (CFST), the dilation behavior of the confined concrete influences the structural member behavior in various ways. Fig. 3a schematically shows a CFST under compression, where the dilation of the confined concrete plays a significant role in the buckling process of the steel tube. The dilation-confinement interaction could also be further complicated by the combination of multiple confining devices/materials. For instance, a CFST member with an inner FRP tube (e.g., [48,49])

is schematically shown in Fig. 3b. The concrete sandwiched between the external steel tube and the inner FRP tube is under a complicated form of confinement; and meanwhile, the inner concrete core is subjected to the combined confinement of the inner tube, sandwiched concrete, and external tube. Other examples of structural members with multiple sources of confinement abound, such as CFSTs with inner steel spirals (e.g., [50–52]) and FRP-concrete-steel double-skin tubular (DST) members where the concrete is sandwiched between an inner steel tube and an outer-FRP skins [24,53].

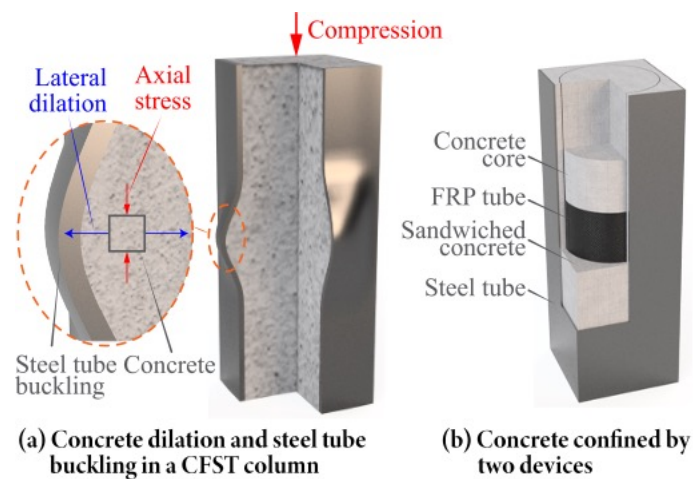


Fig.3 Interactions between concrete and confining devices

This paper presents a plasticity constitutive model that can closely predict the 3D stress-strain behavior of concrete under all forms of active and passive confinement, covering both uniform and non-uniform confinement scenarios. The components of the existing plasticity models which are compatible with confined concrete behavior are employed in the current model, while novel components for the deviatoric dilation behavior of non-uniformly confined concrete are devised. The details of the proposed model are given in the next section, followed by its calibration with available experimental data. Its implementation in the general-purpose FE code ABAQUS is

explained subsequently. Finally, the performance of the proposed model is evaluated against experimental data for compressed concrete under various confining conditions, which demonstrates its high accuracy.

2. Constitutive equations

The proposed model is based on the theory of incremental plasticity under the assumptions of small strains, isothermal conditions, and rate independence. The incremental stress-strain relationship is $\dot{\boldsymbol{\sigma}} = D: (\dot{\boldsymbol{\varepsilon}} - \dot{\boldsymbol{\varepsilon}}_p)$, where $\boldsymbol{\sigma}$ is the stress tensor, D is the elastic stiffness tensor, $\boldsymbol{\varepsilon}$ and $\boldsymbol{\varepsilon}_p$ are the total and the plastic strain tensors respectively that meet the strain decomposition requirement that $\dot{\boldsymbol{\varepsilon}} = \dot{\boldsymbol{\varepsilon}}_e + \dot{\boldsymbol{\varepsilon}}_p$, where $\boldsymbol{\varepsilon}_e$ is the elastic strain tensor and the superimposed dot denotes increments. A yield surface $f(\boldsymbol{\sigma}; \kappa) = 0$ and a potential surface $g(\boldsymbol{\sigma}; \kappa) = 0$ in the stress space are employed to describe the strength and deformation behavior of concrete, respectively. Their evolution due to plastic flow is determined by the hardening/softening rule $\dot{\kappa} = \dot{\kappa}(\dot{\boldsymbol{\varepsilon}}_p)$, where κ is the internal state variable (ISV). The yield surface, potential surface, and hardening/softening rule of a series of representative concrete plasticity models are summarized in Table 1. The details of these components are discussed in the subsequent sub-sections, in contrast with the experimental observations for confined concrete.

Table 1 A summary of representative plasticity-based constitutive models for concrete

Plasticity-based models	Strength and yield surfaces		Potential surface		Hardening/softening rule: Internal state variable
	Base surface	Capped or not	Meridian	Deviatoric	

Han and Chen [25]	Willam-Warnke	Capped	Straight	Circular	Plastic work
Pietruszczak et al. [54]	Willam-Warnke-like	Not	Capped	Associative	Plastic deviatoric strain length (factored)
Lubliner et al. [55]	Mohr-Coulomb	Not	Straight	Associative	Plastic work
Lee and Fenves [26]	Willam-Warnke-like with straight meridians	Not	Straight	Circular	Plastic work
Etse and Willam [56]	Willam-Warnke	Capped	Capped	Associative	Plastic strain length (factored)
Grassl et al. [27]	Menetrey-Willam	Not	Curved open	Circular	Plastic volumetric strain
Papanikolaou and Kappos [28]	Menetrey-Willam	Not	Curved open	Trefoil	Plastic volumetric strain
Piscesa et al. [45]	Menetrey-Willam	Not	Curved open	Circular	Plastic volumetric strain
Paliwal et al. [29]	Menetrey-Willam	Capped	Capped	Associative	Plastic strain length (factored)

To achieve transformation-independence and convenient mathematical expressions, the model is constructed based on the three stress invariants: the hydrostatic stress invariant (ξ), the deviatoric stress invariant (ρ), and the deviatoric polar angle, or the Lode-angle (θ), which form the well-known Haigh–Westergaard coordinate system. Their algebraic relationships with the principal stresses are given in Appendix A, and their geometric orientations in the principal stress space are shown in Fig. 4a. The $\rho - \xi$ planes, where $\theta = \text{constant}$, are referred to as the Rendulic planes (Fig. 4b), and the $\rho - \theta$ planes, where $\xi = \text{constant}$, are referred to as the deviatoric

planes (Fig. 4c). The intersections of the yield and the potential surfaces with the Rendulic planes are the meridians, and the intersections with the deviatoric planes are the deviatoric traces.

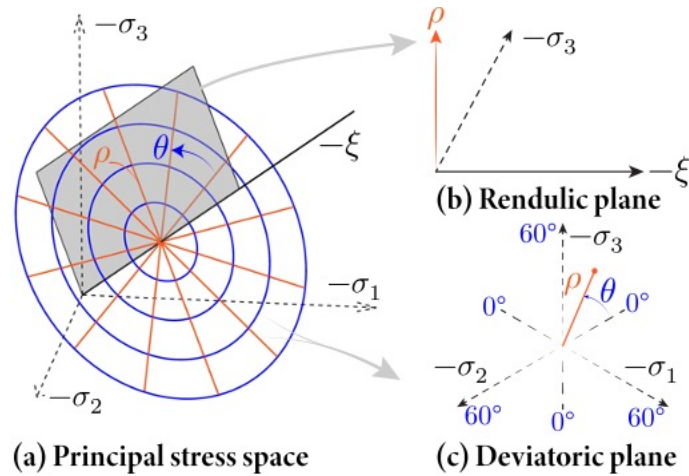


Fig.4 The Haigh–Westergaard coordinate system

2.1 Strength and yield surfaces

The multiaxial strength behavior of concrete is generally path-independent [1,2,54], and plasticity models with open cone-like strength surfaces (e.g., [3,4,54,55]), despite their slight differences in meridians and deviatoric traces, all predict the concrete strength behavior well under either active or passive confinement. The strength surface proposed in Menetrey and Willam [3] has been adopted in many plasticity-based models (see Table 1) (e.g., [27,29,57]), and combined with the Rankine cut-off to form a plasticity-fracture strength surface [58]. This strength surface is employed as the envelope of the yield surfaces in the present model. It should be noted that in the present paper, the term “transition” is used to refer to the state of concrete reaching the strength surface, after which the concrete may exhibit either a softening or hardening stress-strain response in the predominant compressive stress direction depending on the nature and level of

the other compressive stresses (i.e., confinement). The term “peak” is not adopted herein as a hardening axial stress-strain response is often displayed by concrete under passive confinement.

It is well-established that, for concrete, the yield surface/condition is merely a convenient definition to facilitate mathematical modeling. Therefore, for the pre-transition regime of concrete, open yield surfaces similar to the open strength surface with reduced sizes, also referred to as base yield surfaces, have been employed in many plasticity models (e.g., [27,28,54,55]); the meridians of such base yield surfaces are schematically shown in Fig. 5 on the Rendulic plane. In other plasticity models, additional caps are employed together with base yield surfaces to form closed yield surfaces (e.g., [25,29,56,59,60]); the meridians of the caps are schematically shown as the dashed curves in Fig. 5. For civil engineering applications where the concrete is generally under passive confinement, the minimum principal stress is dominant in magnitude, and the stress-path generally intersects the base yield surfaces but not the caps, as schematically indicated in Fig. 5.

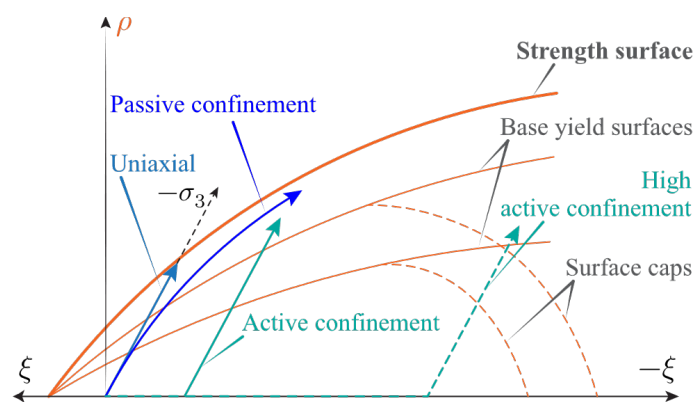


Fig.5 Schematic of stress-paths and meridians of yield surfaces

Therefore, the caps of the yield surfaces are irrelevant for the modeling of such structural members; they are only relevant for concrete with such a high active confinement level that the stress-path is likely to intersect the yield surface caps as indicated in the figure. Consequently, the more straightforward open yield surfaces [27,28] are sufficient for the purposes of the current model, and their mathematical expression is as follows:

$$f(\xi, \rho, \theta; \kappa) = \left(\sqrt{1.5} \frac{\rho}{h(\kappa) \cdot f_c} \right)^2 + m(\kappa) \left(\frac{\rho}{\sqrt{6} \cdot h(\kappa) \cdot f_c} r(\theta) + \frac{\xi}{\sqrt{3} \cdot h(\kappa) \cdot f_c} \right) - c(\kappa) = 0 \quad (1)$$

where κ is the internal state variable (ISV), f_c is the uniaxial compressive strength, f_t is the uniaxial tensile strength, and h and c are the hardening and softening functions that are no greater than unity. The strength surface is obtained when both h and c are equal to unity. The friction parameter m and the deviatoric shape function r have the following expressions:

$$m(\kappa) = 3 \frac{(h(\kappa) \cdot f_c)^2 - f_t^2}{h(\kappa) \cdot f_c \cdot f_t} \cdot \frac{e}{e+1} \quad (2)$$

$$r(\theta) = \frac{4(1-e^2) \cos^2 \theta + (2e-1)^2}{2(1-e^2) \cos \theta + (2e-1) \sqrt{4(1-e^2) \cos^2 \theta + 5e^2 - 4e}} \quad (3)$$

where the parameter e describes the out-of-roundness of the deviatoric trace of the yield surface: a value of 0.5 defines a triangular trace, and 1.0 circular. The 3D visualization of the strength and yield surfaces in the principal stress space is presented in Fig. 6a. The two inner surfaces are yield surfaces corresponding to $h = 0.3$ and 0.6, and the envelope is the strength surface when $h = 1$. Fig. 6b shows their intersections with the deviatoric plane at $\xi = -0.5f_c$. Fig. 6c shows their meridians on the Rendulic planes of $\theta = 60^\circ$ and 0° in the pre-transition (left) and post-transition (right) regimes. On the left, the yield surface ‘opens up’ with the increase of h , representing the material hardening process. On the right, the de-cohesion process is represented by the shift of the yield surface along the hydrostatic axis.

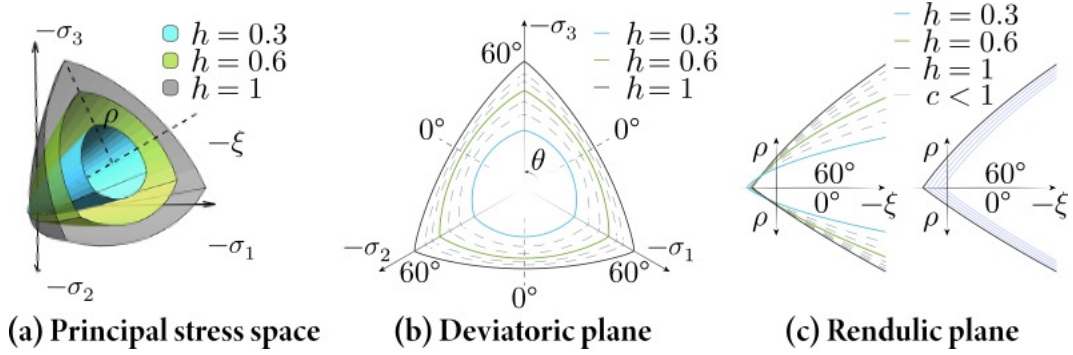


Fig.6 Visualization of the strength and the yield surfaces

2.2 Potential surface: volumetric components

The potential surface determines the direction of the plastic strain increment: $\dot{\boldsymbol{\varepsilon}}_p = \lambda \mathbf{g}_\sigma$, where λ is the plastic multiplier, and $\mathbf{g}_\sigma = \partial g / \partial \boldsymbol{\sigma}$ is the normal of the potential surface (flow direction). The plastic strain can be decomposed into a volumetric component projected on the hydrostatic axis, $\dot{\boldsymbol{\varepsilon}}_p^v = I_1(\dot{\boldsymbol{\varepsilon}}_p) / \sqrt{3} = \xi(\dot{\boldsymbol{\varepsilon}}_p)$, and a deviatoric component projected on the π -plane, $\dot{\boldsymbol{e}}_p = \dot{\boldsymbol{\varepsilon}}_p - \dot{\boldsymbol{\varepsilon}}_p^v$; the direction of $\dot{\boldsymbol{\varepsilon}}_p^v$ involving ξ can be determined in the $\rho - \xi$ plane by the meridians of the potential surface, and $\dot{\boldsymbol{e}}_p$ involving ρ and θ can be determined in the $\rho - \theta$ plane by the deviatoric traces of the potential surface. Therefore, the proper modeling of the deformational behavior of concrete consists of the proper description of the plastic volumetric and deviatoric behaviors.

The plastic volumetric behavior of concrete is characterized by hydrostatic pressure-dependent plastic volumetric dilation and compaction, which stems from its frictional and porous microstructure [61–63]. Specifically, macroscopic dilation may arise from sliding on the surfaces of microscopic cracks with asperities [61,62], and macroscopic compaction may result from the

collapse of porous microstructures [64]. Therefore, concrete may potentially undergo plastic volumetric compaction, conservation, or dilation, depending on the stress path.

Experimental data indicate that, in the pre-transition regime, the concrete plastic volumetric strain *increment* undergoes a negative-to-positive process [1,2,13,20,32,65]. This can be interpreted as follows: the plastic Poisson's ratio (defined in the same way as the elastic Poisson's ratio but for the plastic strains) of concrete is close to the elastic Poisson's ratio at the beginning of plastic deformation, and gradually increases as the plastic deformation accumulates [19]. The physical explanation is that the plastic deformation process is a gradual evolution from the generation to the coalescence of microcracks [66–68].

In the post-transition regime, concrete exhibits different volumetric behaviors for different stress paths. A comprehensive study of concrete under active confinement of various levels was conducted by Samani and Attard [69]. The results indicate that concrete basically undergoes plastic volumetric dilation, except that, under a very high level of confinement, it exhibits plastic volumetric conservation. On the other hand, experimental data of passively-confined concrete were reviewed by Lim and Ozbakkaloglu [70] and Piscesa et al. [45], and their analyses agreed that, under a low level of passive confinement, concrete undergoes plastic volumetric dilation, and, under a high level of passive-confinement, concrete undergoes a process of plastic volumetric dilation that then transitions to plastic volumetric compaction. Taken collectively, a valid plasticity model for confined concrete should be able to predict both plastic volumetric dilation and compaction as well as pressure dependence.

The Drucker-Prager (D-P) (e.g., [25,26,32]) and the Mohr-Coulomb (e.g., [55]) potential surfaces are characterized by straight meridians, as shown in Fig. 7. Therefore, the potential-surface normal directions at different pressure levels ξ_1 , ξ_2 , and ξ_3 are the same and the direction of the plastic volumetric strain vector is not ξ -dependent. To describe pressure-sensitive dilation behavior, the slope of the meridian needs to be related to the pressure level, such as the approach adopted in Bao et al. [30], Jiang and Wu [36], Mohammadi et al. [37], and Yu et al. [34]. For D-P type potential surfaces having hyperbolic meridians, the potential-surface normal direction varies at low hydrostatic pressure levels (ξ_1 and ξ_2 in the figure), but remains nearly unchanged when the pressure level is high (ξ_3 in the figure) (e.g., [38,71]). A polynomial potential surface has curved meridians, which leads to different potential-surface normal directions for different pressure levels (e.g., [27,28,58,59,72]). While the plasticity models having hyperbolic or polynomial meridians are able to predict pressure dependence, they are mathematically unable to predict potential-surface normal directions that lead to plastic volumetric compaction, as indicated in the figure.

The model developed by Piscesa et al. [45,57] employs a potential surface with parabolic (a special case of the polynomial) meridians, which are open to the negative direction of the hydrostatic axis as indicated in Fig. 7 (i.e., $-\xi$, to the right of the origin in the figure). To overcome the limitation in predicting plastic volumetric compaction, the opening direction of the parabolic meridian is reversed to the positive direction of the hydrostatic axis (i.e., ξ , to the left of the origin in the figure) when needed so that the normal direction of the potential surface becomes compatible with plastic volumetric compaction, as schematically indicated by the dashed meridian. Alternatively, a capped potential surface has meridians intersecting the

hydrostatic axis (e.g., [29,46,54,56]), which can predict the smooth compaction-to-dilation transition for increasing pressure levels, as shown in Fig. 7. The current model adopts a capped meridian similar to those adopted in Farahmandpour et al. [46] and Pietruszczak et al. [54] as follows:

$$g(\xi, \rho; \kappa) = \rho + A \cdot (B \cdot f_c - \xi) \cdot \ln \frac{B \cdot f_c - \xi}{\xi_0} = 0 \quad (4)$$

where $A \equiv A(\kappa)$ and $B \equiv B(\kappa)$ control the shape of the meridian, and ξ_0 is a dependent coefficient ensuring that the stress point dwells on the potential surface, i.e., its value ensures $g(\xi, \rho; \kappa) = 0$.

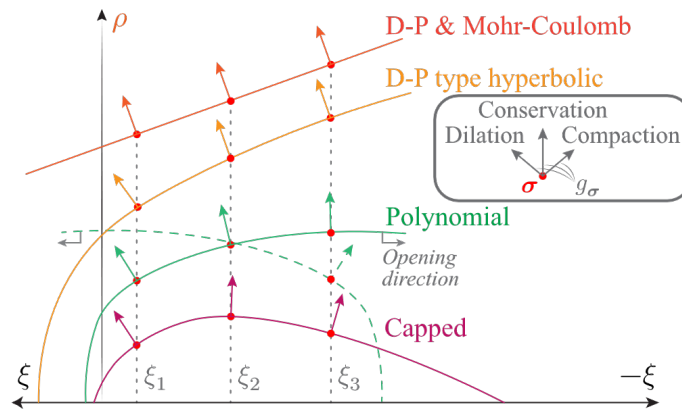


Fig.7 Meridians of potential surfaces and their normal directions at different pressures

The meridians of potential surfaces with varying values of A and B on the Rendulic plane are shown schematically in Fig. 8a and b, respectively. Such a meridian is convex and intersects the negative hydrostatic axis at $(\rho = 0, \xi = B \cdot f_c - \xi_0)$, but it does not intersect the positive hydrostatic axis although it approaches the point $(\rho = 0, \xi = B \cdot f_c)$ on the positive hydrostatic axis (i.e., to the left of the origin in Fig. 8a). The meridian is divided by a critical line ($\rho = A \cdot (B \cdot f_c - \xi)$), shown as a dashed line in the figure, into two segments. If the stress point dwells

on the left segment, it indicates plastic volumetric dilation (see the set of meridian, critical line, and potential-surface normal direction with violet color and thick line weight in the figure); if it is on the right segment, plastic volumetric compaction (see the set of meridian, critical line, and potential-surface normal direction with bluish color and thick line weight in the figure). The intersecting point between the meridian and the critical line is then the point of plastic volumetric conservation. Parameter A controls the critical line slope and hence the plastic volumetric behavior at a stress point. A higher value of A corresponds to a smaller dilation. Parameter B controls the location of the asymptotic vertex on the positive hydrostat, as shown in Fig. 8b.

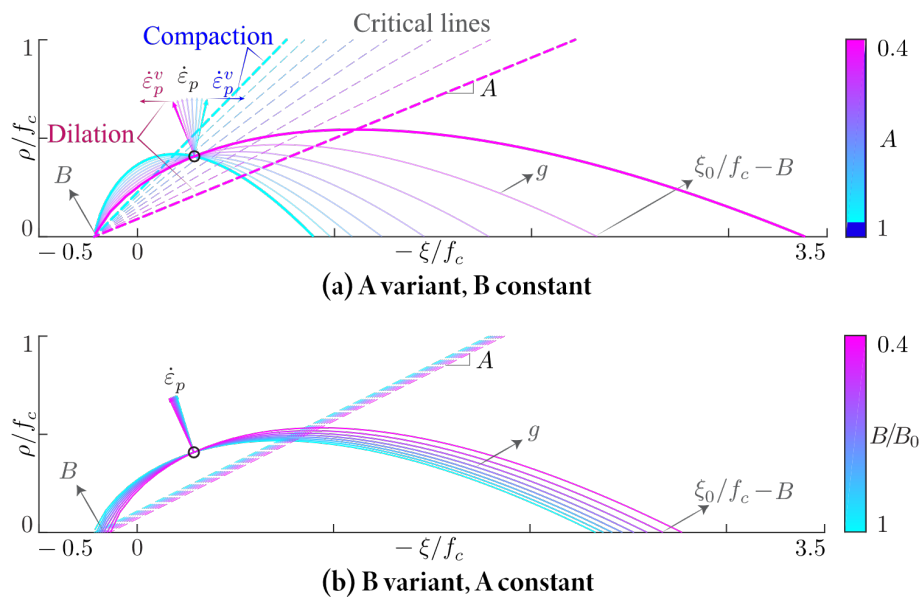


Fig.8 Meridians of potential surfaces

2.3 Potential surface: deviatoric components

The plastic deviatoric behavior of concrete has been less investigated than its volumetric counterpart. Therefore, the simplest θ -independent potential surface has been widely accepted

(e.g., [26,30,34,36,44,45,55,59,72,73]). It has a circular deviatoric trace, which can be expressed by a constant normalized polar length ($\bar{\rho}$): $\bar{\rho}(\theta) = \rho(\theta)/\rho(60^\circ) = 1$, as shown in Fig. 9a. The direction of the deviatoric component of the plastic strain increment $\dot{\epsilon}_p$ for a stress point $[\rho, \xi, \theta]$ is normal to the deviatoric trace; the direction can be represented by a Lode-angle equal to ϑ as indicated by the green dashed arrow in the figure. Its components in the principal directions are denoted by $\dot{\epsilon}_p^1$, $\dot{\epsilon}_p^2$, and $\dot{\epsilon}_p^3$. For the case of concrete under either active [69] or passive uniform confinement [45], where $0 > \sigma_1 = \sigma_2 > \sigma_3$ and $\theta = 60^\circ$, it has $\dot{\epsilon}_p^1 = \dot{\epsilon}_p^2 > \dot{\epsilon}_p^3$. Therefore, the circular trace giving $\dot{\epsilon}_p^1 = \dot{\epsilon}_p^2$ at $\theta = 60^\circ$ is accurate (see Appendix B for details).

However, for concrete under non-uniform confinement where $\sigma_1 > \sigma_2 > \sigma_3$ and $\theta < 60^\circ$, it has $\dot{\epsilon}_p^1 > \dot{\epsilon}_p^2$ and hence $\epsilon_1 > \epsilon_2$ as shown in Fig. 2e. In this case, the accurate prediction of the difference between ϵ_1 and ϵ_2 is critical. For any stress vector with a Lode angle θ and the corresponding potential-surface normal direction (with a Lode angle of ϑ), the circular trace is limited in describing the difference between $\dot{\epsilon}_p^1$ and $\dot{\epsilon}_p^2$ because $\vartheta = \theta$: the deviatoric dilation behavior is not adjustable. Consequently, a suitable potential deviatoric trace for non-uniformly confined concrete should have an *adjustable* potential-surface normal direction relative to the stress vector direction, i.e., $\vartheta \equiv \vartheta(\theta; \kappa)$. Moreover, the predicted deviatoric dilation behavior using the circular trace for non-uniformly confined concrete shows a much smaller difference than that observed in experiments [37,39]. Generally, the smaller is ϑ , the larger is the predicted difference (see Appendix B for details). Therefore, the adjustable $\vartheta(\theta; \kappa)$ should generally satisfy $\vartheta < \theta$ based on the current available pertinent experimental data.

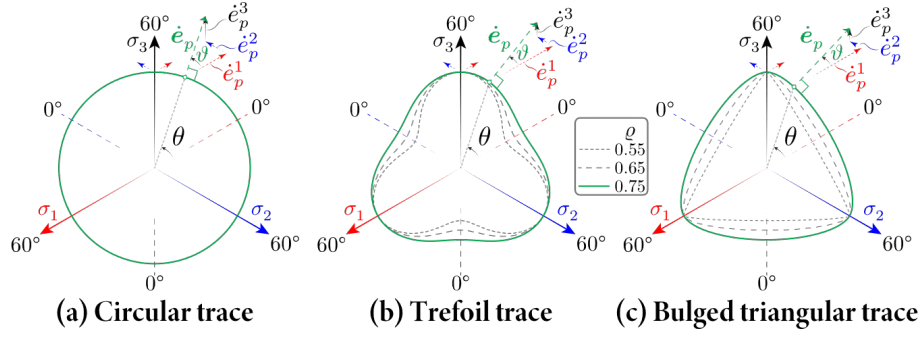


Fig.9 Effect of deviatoric trace on plastic strain increment direction under non-uniform confinement

Such a θ -dependent deviatoric trace with a trefoil shape has been proposed by Papanikolaou and Kappos [28], which can be approximated by the following mathematical form of the normalized polar length:

$$\bar{\rho}(\theta) = \left(\rho + \frac{(1-\rho)(\cos(\pi-3\theta)+1)}{2} \right) \quad (5)$$

where $\rho = \rho(0^\circ)/\rho(60^\circ) \leq 1$ is a prescribed value that determines the shape of the trace. Fig. 9b plots three such trefoil traces for $\rho = 0.55, 0.65,$ and 0.75 . It is seen that although the shape is adjustable by varying ρ , the trace remains highly rounded near $\theta = 60^\circ$, indicating $\vartheta \approx \theta$, while it becomes concave ($\vartheta < 0^\circ$) around $\theta = 0^\circ$. For structural applications, non-uniformly confined concrete is most likely to be represented by a stress state near $\theta = 60^\circ$. Therefore, this trefoil deviatoric trace provides a very limited adjustment range for the deviatoric dilation behavior. Further, when ρ is small enough to induce concavity, the model may become numerically problematic and result in negative plastic energy dissipation (see Appendix B for details). Therefore, this trefoil trace may not be suitable for describing non-uniformly confined concrete, although it is adjustable and gives $\vartheta < \theta$.

It has been suggested that the associativity of the plastic potential function with the yield function should be maintained in the deviatoric direction for concrete plasticity models [56,62,63], which results in a bulged-triangular deviatoric trace for the potential function as adopted in Paliwal et al. [29]. In the present model, this basic shape is adopted but with an evolution rule with respect to plastic deformation derived from a new interpretation of experimental observations. Accordingly, the potential-surface deviatoric shape is expressed as: $\bar{\rho}(\theta) = 1/r(\theta, \varrho)$, where $r(\theta, \varrho)$ is the same shape function as that in the yield function except that ϱ is used to substitute e . Fig. 9c shows the bulged-triangular traces for $\varrho = 0.55, 0.65, \text{ and } 0.75$. It is seen that these traces are characterized by a pointed tip indicating $\vartheta \ll \theta$ near $\theta = 60^\circ$ while they remain rounded ($\vartheta \approx \theta > 0^\circ$) near $\theta = 0^\circ$. As a result, ϑ is highly adjustable and decreases rapidly near $\theta < 60^\circ$, and remains convex near $\theta = 0^\circ$ (see Appendix B for details). These features are ideal for the description of the deviatoric dilation behavior of concrete.

By putting together the volumetric and the deviatoric components, the complete proposed potential function with θ -dependence is therefore as follows:

$$g(\xi, \rho, \theta; \kappa) = r(\theta, \varrho(\kappa)) \cdot \rho + A(\kappa) \cdot (B(\kappa) \cdot f_c - \xi) \cdot \ln \frac{B(\kappa) \cdot f_c - \xi}{\xi_0} = 0 \quad (6)$$

where $A(\kappa)$, $B(\kappa)$, and $\varrho(\kappa)$ control the evolution of the potential function with the accumulation of plastic damage as calibrated in Section 3. A 3D visualization of the potential surface is shown in Fig. 10. For concrete in the intact stage, ϱ tends to have a large value, and the potential surface is plump as shown in Fig. 10a; for concrete in a late stage of plastic deformation, ϱ tends to approach e , and the potential surface is angular as shown in Fig. 10b. The detailed experimental calibration is discussed in Section 3.

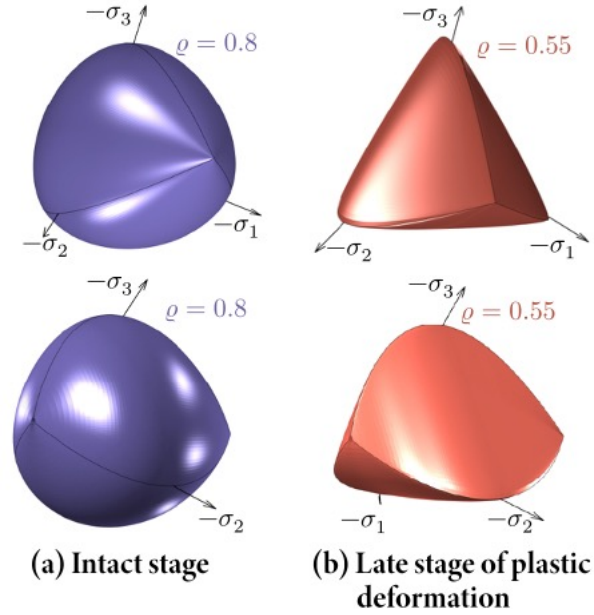


Fig.10 Proposed θ -dependent potential surface for concrete at different stages of plastic deformation

2.4 Internal state variable and hardening/softening function

The evolution of the yield and the potential surfaces is driven by the accumulation of plastic damage, which is represented by the internal state variable (ISV) κ that is irreversible ($\dot{\kappa} \geq 0$). In some models, the ISV is related to the plastic work that involves both stresses and plastic strains (e.g., [25,26,55,60]), while in other models, it is related to only plastic strains, which is mathematically more straightforward. It is taken by some researchers as the plastic volumetric strain ($\dot{\kappa} = \dot{\varepsilon}_p^v$) (e.g., [27,28,58]) with the consideration that ε_p^v by itself is a direct measure of plastic damage. However, this poses a natural limit to modeling plastic volumetric compaction ($\dot{\varepsilon}_p^v < 0$), since $\dot{\kappa} = \dot{\varepsilon}_p^v \geq 0$. While this problem is circumvented by using a factored plastic volumetric strain as ISV [45], it is numerically complicated.

In Etse and Willam [56], Grassl and Jirásek [59], Jiang and Wu [36], Karabinis and Rousakis [33], and Rousakis et al.[32], the ISV is taken as the plastic strain length scaled by a ductility measure. An ISV of this kind is compatible with plastic volumetric compaction and straightforward in using the ductility measure to represent pressure sensitivity. In the present model, the ISV increment is taken to be the length of plastic strain increment scaled by a ductility measure (χ_p), which accounts for the influence of confinement on the ductility of concrete as adopted in Farahmandpour et al. [46] and Grassl et al. [72]. Its accumulation is governed by the following relationship:

$$\dot{\kappa} = \frac{\|\dot{\boldsymbol{\varepsilon}}_p\|}{\chi_p(\boldsymbol{\sigma})} \quad (7)$$

where $\|\dot{\boldsymbol{\varepsilon}}_p\| = \sqrt{\dot{\boldsymbol{\varepsilon}}_p : \dot{\boldsymbol{\varepsilon}}_p}$ is the Euclidean norm of the plastic strain increment. The calibration of χ_p is given in Section 3.5.

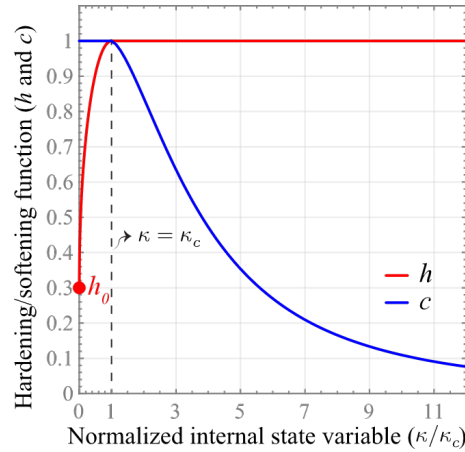
The transition state of concrete is defined by a critical value of $\kappa = \kappa_c$. As a result, the hardening function must be such that when $\kappa = 0$, it assumes an initial value determining the initial yield surface, i.e., $h = h_0$, and when $\kappa = \kappa_c$, $h = 1$ to represent the strength surface. Based on the characteristics of stress-strain curves from uniaxial compression tests of concrete (see Fig. 1b), the hardening function generally takes a form that has a steep slope at the onset of plastic flow ($h = h_0$) followed by a zero slope at the transition state ($h = 1$), though the specific mathematical forms may be different [27,28,30,44,56]. In the post-transition stage, it maintains a value of unity. The hardening function in the current model is adopted from Etse and Willam [56]:

$$h(\kappa) = h_0 + (1 - h_0) \sqrt{1 - \left(1 - \frac{\kappa}{\kappa_c}\right)^2}, \kappa \leq \kappa_c \quad (8)$$

In the post-transition regime, it is a characteristic that the strength decreases with a small slope at the beginning and approaches zero asymptotically. Therefore, the softening function assumes the following form that is modified from Papanikolaou and Kappos [28]:

$$c(\kappa) = \left(1 + \left(\frac{\kappa - \kappa_c}{\kappa_s}\right)^{1.5}\right)^{-1.5}, \kappa \geq \kappa_c \quad (9)$$

where κ_s controls the descending rate of the softening branch. A schematic plot of the hardening and softening functions is shown in Fig. 11. The adopted softening function approaches zero asymptotically instead of a distinct failure criterion. Nevertheless, a numerical threshold of $c_{min} = 1 \times 10^{-3}$ may be taken as the failure condition. For confined concrete, failure of the confining material generally precedes this failure condition for concrete.



3. Model calibration

The proposed model is aimed at describing the behavior of concrete with a minimal number of input parameters. By default, only the uniaxial compressive strength (f_c) is needed. However, better predictions can be achieved if more parameters such as the uniaxial tensile strength (f_t), the axial strain at the unconfined uniaxial compressive strength (ε^k), and the descending parameter (κ_s) are directly defined. This flexibility of parameter definition makes the model highly adaptable: when more comprehensive experimental data become available, the calibration can be accordingly updated. The present model defines compressive values as negative values, except for the material strengths, which are all given in positive values to comply with the widely accepted convention.

3.1 Strength-related parameters

The strength surface is defined by the three strength parameters of concrete: f_c , f_t , and the equibiaxial compressive strength (f_{bc}). When experimental data of f_t are not available, it can be estimated by $f_t = 0.53\sqrt{f_c}$ MPa as given in Wight and MacGregor [74]. Specifically, the Menetrey-Willam failure surface may exhibit moderate inaccuracy when used for both tension- and compression-dominant stresses, and improvement of the friction parameter has been proposed in Piscesa et al. [47]. As a convenient compromise, for compression-dominant stress conditions, adjusting the value of f_t/f_c is practically equivalent to adjusting the friction parameter leading to a spurious value of the uniaxial tensile strength (\bar{f}_t), which has no influence if the focus of the analysis is on compression-dominant cases. The value of f_{bc} has been widely accepted to be approximately $1.15f_c$ based on the experimental work by Kupfer et al. [2] on normal strength concrete, but it has also been reported that the value of f_{bc}/f_c reduces when the

concrete strength increases [75]. As a result, the following equation proposed by Papanikolaou and Kappos [28] is suggested for use to provide closer estimates of f_{bc}/f_c for a wider range of concrete strengths: $f_{bc} = 1.5f_c^{-0.075} \cdot f_c$. The deviatoric shape parameter e is then determined by the following equation [59]:

$$e = \frac{1+e'}{2-e'}, e' = \frac{f_t(f_{bc}^2 - f_c^2)}{f_{bc}(f_c^2 - f_t^2)} \quad (10)$$

The Poisson's ratio for concrete is normally taken as a constant falling within the range of 0.15 to 0.2 (e.g., [76–78]). It is noted that the influence of the value of Poisson's ratio on the predicted dilation behavior of concrete is limited in a plasticity model since the plastic deformation is dominant. As a result, a constant value of 0.18 is adopted herein for the elastic Poisson's ratio. By contrast, the total axial strain at the transition uniaxial compressive stress (ε^k) has a larger influence on the dilation behavior of concrete. When experimental data are unavailable for ε^k , its value can be estimated from the equation proposed by Tasdemir et al. [79], which was based on test data for concrete uniaxial compressive strengths ranging from 6 to 105 MPa:

$$\varepsilon^k = (0.067f_c^2 - 29.9f_c - 1053) \times 10^{-6} \quad (11)$$

Since the relationship between ε^k and f_c is rather scattered, many other empirical equations are available (e.g., [28,80,81]), but Eq. (11) appears to have been relatively more widely used [82,83]. Similarly, the elastic modulus is suggested to be estimated from the following equation given in ACI Committee 318 [84] when test data are not available:

$$E = 4730\sqrt{f_c} \text{ MPa} \quad (12)$$

Obviously, other empirical equations for concrete material parameters may be used when test data are unavailable, as long as their accuracy can be demonstrated.

3.2 Potential-surface volumetric parameters in the pre-transition regime

In the present paper, the plastic volumetric behavior is described by the potential angle (β), dilation angle (α), and plastic Poisson's ratio (ψ); since the former two terms have different definitions in different studies, clarification is given in Appendix C. In general, the plastic Poisson's ratio in the pre-transition regime is monotonically increasing between the initial state (denoted by '0') and the transition state (denoted by 'k'). The initial plastic Poisson's ratio is suggested to be identical with the elastic Poisson's ratio, i.e. $\psi_0 = \nu$, based on the investigations in Candappa et al. [19] and Piscesa et al. [45]. This is microscopically reasonable, considering that the plastic behavior deviates gradually from the elastic behavior along with the initiation of microcracks.

At the transition state, the total volumetric strain ($\varepsilon^{v,k} = I_1(\boldsymbol{\varepsilon}^k)$) of concrete is suggested as $\varepsilon^{v,k} = 0$ by Imran and Pantazopoulou [1], which has been widely adopted (e.g., [28,45]). Fig. 12a shows the normalized transition-state volumetric strain ($\varepsilon^{v,k}/\varepsilon^{k,*}$) against the normalized confining stress ($-\sigma_l/f_c^*$) (where $\varepsilon^{k,*}$ and f_c^* are the axial transition strain and compressive strength under active confinement) for uniform active confinement based on the data extracted from Candappa et al. [19], Lahlou et al. [85], Lim and Ozbakkaloglu[70], Lu and Hsu [86], and Sfer et al. [87]. It is seen that the confidence intervals ('C.I. in the figure') cover a large area rather than being closely packed, and the center of confidence interval (i.e., the sample mean value) is generally greater than zero and increases as the level of confinement reduces. As a result,

it is reasonable to assume that the total volumetric strain at the transition uniaxial compressive stress $\varepsilon^{v,k} = 0.2 \sim 0.8 \varepsilon^k$ rather than the widely adopted $\varepsilon^{v,k} = 0$.

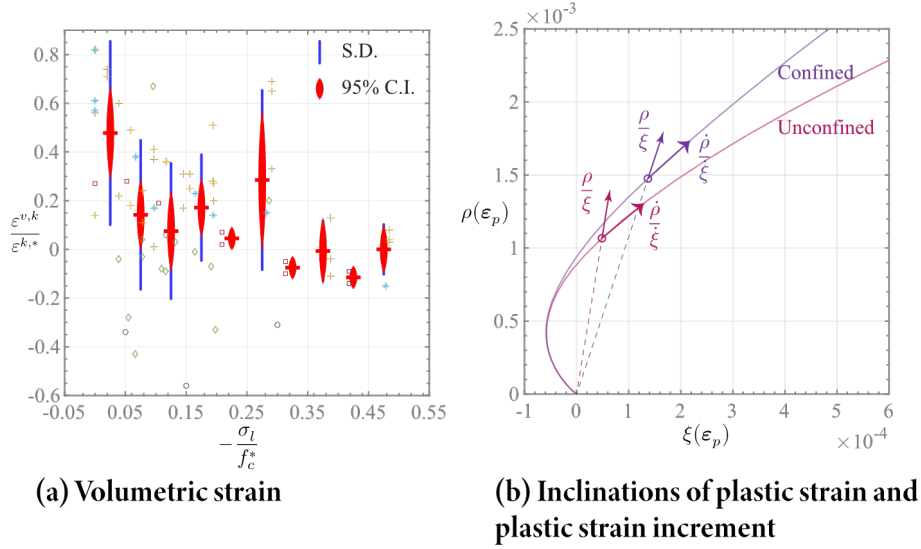


Fig. 12 Plastic volumetric behavior at transition state

However, it is not straightforward to obtain the transition-state plastic Poisson's ratio (ψ_k) from $\varepsilon^{v,k}$. In the models proposed in Grassl et al., [27] and Papanikolaou and Kappos [28], it is simplified that, at the transition state, the inclination of the plastic strain ($\rho(\boldsymbol{\varepsilon}_p^k)/\xi(\boldsymbol{\varepsilon}_p^k)$) is coaxial with the inclination of the plastic strain increment ($\rho(\dot{\boldsymbol{\varepsilon}}_p^k)/\xi(\dot{\boldsymbol{\varepsilon}}_p^k)$). This simplification has the advantage that the former can be easily calibrated from $\varepsilon^{v,k}$ while such calibration is much more difficult for the latter due to the complex evolution of ψ in the pre-transition regime [45]. However, the coaxiality assumption also has the disadvantage of ignoring the obvious difference between the two directions, as illustrated by two example cases of plastic strain evolution for confined concrete and unconfined concrete, respectively (Fig. 12b). It is seen that both cases undergo volumetric compaction followed by volumetric dilation. The transition stress locations

are indicated by the circles on both curves, and the corresponding plastic strain and plastic strain *increment* vectors are indicated at the two transition stress points.

In the present study, a simple assumption is adopted to obtain the relationship between ψ_k and $\varepsilon^{v,k}$ while avoiding both issues mentioned above: since ψ varies monotonically between ψ_0 and ψ_k in the pre-transition regime; it is accordingly assumed that ψ varies linearly between ψ_0 and ψ_k as follows:

$$\psi = \psi_0 + (\psi_k - \psi_0) \left(\frac{\varepsilon_p}{\varepsilon_p^k} \right), h_0 \leq h \leq 1 \quad (13)$$

where $\varepsilon_p^k = \varepsilon^k - \varepsilon_e^k$ and $\varepsilon_e^k = f_c/E$ are the plastic and elastic axial strains at the transition state.

The relationship between the normalized plastic axial strain ($\varepsilon_p/\varepsilon_p^k$) and the normalized plastic Poisson's ratio (ψ/ψ_k) in the pre-transition stage are extracted from the axial stress-strain ($\sigma_3 - \varepsilon_3$) and axial strain-lateral strain ($\varepsilon_3 - \varepsilon_1$) data of unconfined, actively-confined, and FRP-confined concrete tests reported in Lim and Ozbakkaloglu [17] and presented in Fig. 13.

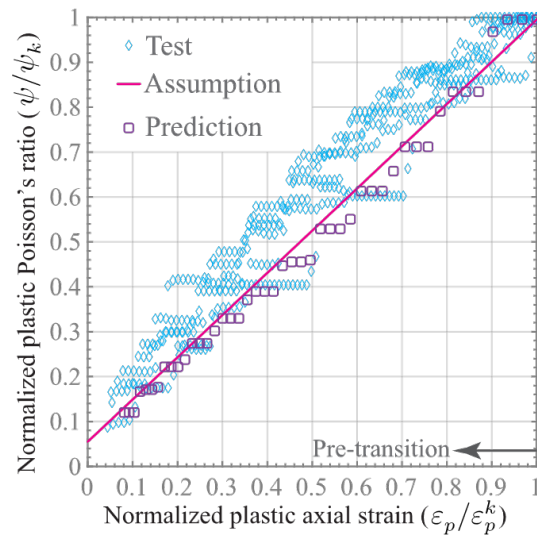


Fig.13 Variation of plastic Poisson's ratio in pre-transition regime

It is seen that the linear assumption agrees well with the experimental data. Based on this linear assumption Eq.(13), $\varepsilon^{v,k} = \int_0^{\varepsilon^k} (2\psi - 1)\dot{\varepsilon}_p + (2\nu - 1)f_c/E$ by definition, and $\psi_0 = \nu$ as discussed above, a rather straightforward relationship can be derived between ψ_k and $\varepsilon^{v,k}$:

$$\psi_k = \frac{\varepsilon^{v,k} - \nu f_c/E + \varepsilon^k(1-\nu)}{\varepsilon^k - f_c/E} \quad (14)$$

Arguably, as shown in Fig.13, a rigorous regression analysis would lead to a nonlinear variation of ψ between ψ_0 and ψ_k . However, due to the large scatter of the experimental data, such a nonlinear representation would hardly increase the accuracy of the predicted pre-transition volumetric dilation behavior while adding complexity to the relationship between ψ_k and $\varepsilon^{v,k}$. Therefore, a linear relationship is adopted in the present study as a good compromise between accuracy and simplicity.

The transition-state plastic Poisson's ratio for concrete of various values of f_c should be in the range of $\psi_k = 0.5 \sim 1.5$ based on the physical meaning of the parameter, with 0.5 indicating plastic volumetric conservation and 1.5 indicating considerable plastic volumetric expansion. Therefore, when experimental data are insufficient to calibrate ψ_k , the median value of $\psi_k = 1.0$ may be used in the proposed constitutive model to achieve a reasonable prediction of the plastic dilation behavior.

This volumetric dilation evolution process as depicted by Eq. (13) is reflected through the evolution of the parameter A in the potential function as follows:

$$A(\kappa) = A_0 + \left(1 - \sqrt{1 - \left(\frac{h-h_0}{1-h_0}\right)^2}\right) (A_k - A_0), \kappa \leq \kappa_c \quad (15)$$

where the relationship between A_0 , A_k and ψ_0 , ψ_k are given in Appendix D. The predicted evolution of plastic Poisson's ratio by Eq. (15) in the pre-transition regime is shown in Fig. 13; it is seen that the linear assumption is well represented by Eq.(15).

3.3 Potential-surface volumetric parameters in the post-transition regime

In the post-transition regime, the plastic volumetric behavior of unconfined and actively confined concrete is characterized by increasing dilation, as pointed out by Samani and Attard [69]. This process is represented by a continuous decrease of the potential parameter A in the post-transition regime, as a smaller value of A corresponds to a larger dilation (see Section 2.2). Further, since $A(\kappa = \kappa_c) = A_k$, the following function describes such an evolution of A in the post-transition regime:

$$A = A^- = A_k \left(1 + \frac{\kappa - \kappa_c}{\kappa_s} \right)^{a^-}, \kappa \geq \kappa_c \quad (16)$$

where A^- denotes the descending value of A in the post-transition regime. The value of a^- controls the rate of decrease for A , as shown in Fig. 14a, and was examined by considering the experimental data of unconfined and actively-confined concretes and the dilation model proposed by Samani and Attard [69]. Fig. 14b shows a representative comparison of the axial-lateral strain relationships of unconfined and actively-confined concretes predicted using various values of a^- with the experimental data and the prediction by Samani and Attard [69]; it is seen that a value of $a^- = -3$ gives reasonable predictions; more validations are given in Section 5.

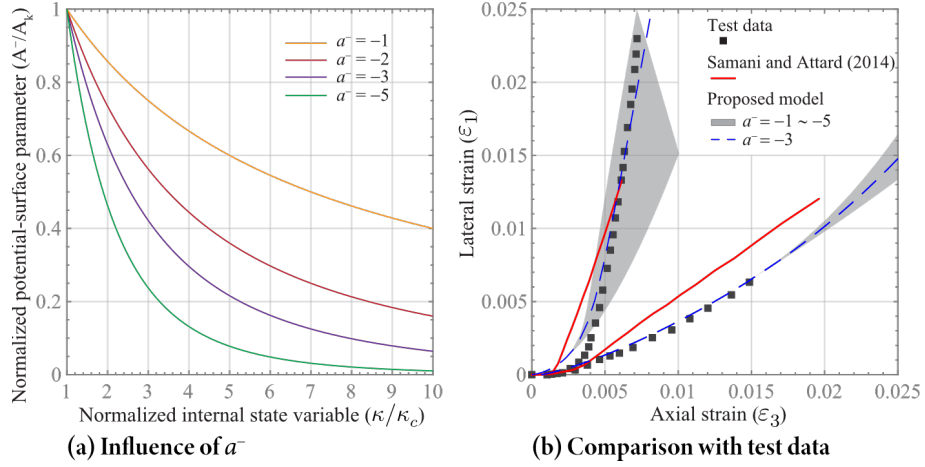


Fig.14 Evolution of potential-surface parameter A in post-transition regime

Further, it has been experimentally observed that passively-confined concrete exhibits a unique phenomenon of dilation, in which an inflection point occurs on the axial-lateral strain curve, or a corresponding turning point on the plastic Poisson's ratio, during the loading process. That is, passively-confined concrete may experience plastic volumetric compaction in the post-transition stage if the confining stresses become sufficiently high. This phenomenon has been quantitatively investigated by Piscesa et al. [45], who proposed that the influence may be approximated as follows in the present nomenclature and notation:

$$\psi = \psi_k + (\psi_0 - \psi_k) \tanh \left(a \left(\frac{\sigma_l}{f_c} \right)^b \right) \quad (17)$$

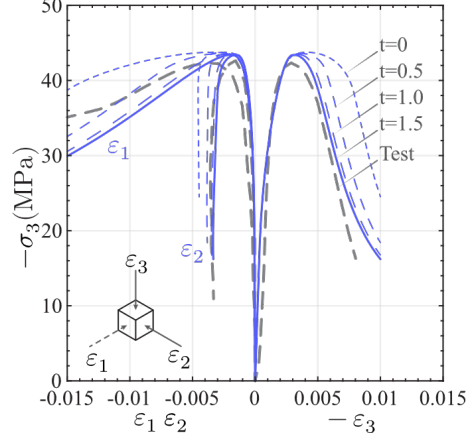
where a and b are constants, and the details can be found in the reference. This relationship is based on a uniform confining stress (σ_l), which loses meaning for non-uniform confinement with unequal confining stresses. Therefore, in order to generalize this relationship to the 3D context of the present model, the confinement level needs to be represented by an invariant confinement measure. Such a measure that has been used to describe the level of confinement in many previous studies (e.g., [46,56,59]) is as follows:

$$\eta = \frac{\langle -\xi/\sqrt{3} - f_c/3 \rangle}{f_c} \quad (18)$$

where ‘ $\langle \cdot \rangle$ ’ denotes the Macaulay bracket. In the present study, this confinement measure is refined to better reflect the reduced confining effect of non-uniform confinement compared to uniform confinement, e.g., the confining effect of $(\sigma_1 = \sigma_2 = \sigma_0)$ is higher than that of $(\sigma_1 = 0, \sigma_2 = 2\sigma_0)$, where σ_0 denotes a specific compressive stress. The refined confinement measure adopted in the present model is then as follows:

$$\eta = \frac{\langle -\xi/\sqrt{3}/r(\theta)^t - f_c/3 \rangle}{f_c} \quad (19)$$

where $r(\theta)$ is greater than unity when the confinement is non-uniform, and t controls the level of confinement reduction due to the non-uniformity. Accordingly, the larger t is, the higher the reduction becomes. Fig. 15 shows the predicted stress-strain curves for a series of values of t (with the values of the other parameters being determined as discussed later) for a highly non-uniform passive confinement scenario. Comparison with the test data indicates that $t = 1.5$ is an appropriate value within the framework of the present model, and the validity of this value is numerically demonstrated in Section 5.3 against the test data of concrete under various non-uniform confinement scenarios where σ_3 is dominant. If the value of t is taken as a larger value, it is possible that the predicted confinement reduction due to non-uniformity is excessive, which may result in erroneous predictions for concrete under very high level of non-uniform confinement (e.g., nearly biaxial compression where $\sigma_1 \gg \sigma_2 \approx \sigma_3$). Therefore, the value of t is conservatively taken as 1.5 in the present model until more experimental data are available and indicate otherwise.

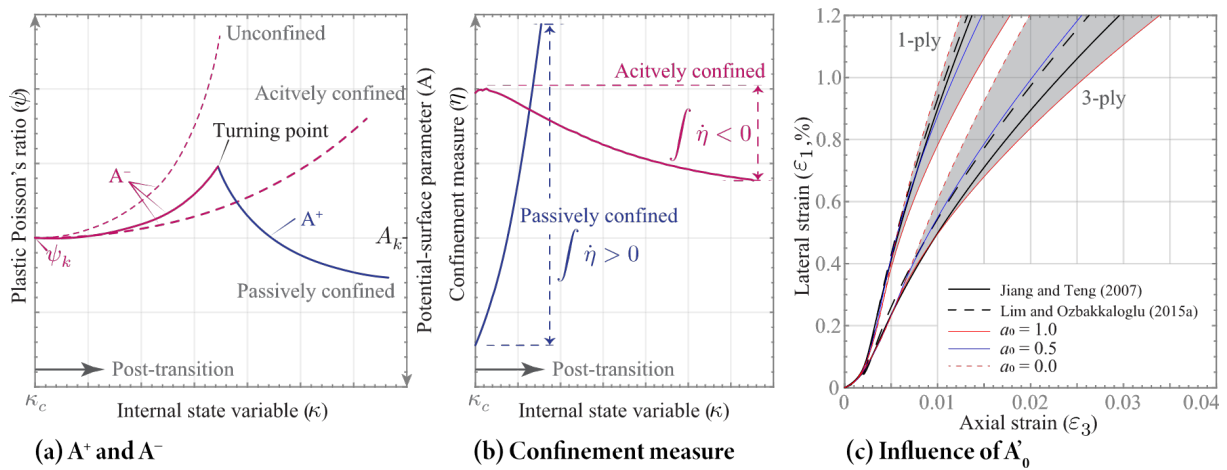


In the present model, the inflected dilation phenomenon for passively-confined concrete is represented by an increasing potential-surface parameter A^+ , as opposed to A^- (Eq.16). A schematic illustration of the relationship between A^+ and A^- is shown in Fig. 16a. It shows that in the post-transition regime, the dilation (represented by ψ) for both unconfined and actively-confined concrete increases monotonically (represented by A^-), while that for the (sufficiently) passively-confined concrete only increases up to a turning point, after which the confining stress is large enough to decrease the dilation (represented by A^+). The results predicted by Eq. (17) are reflected in the present model through the following equation of potential-surface parameter A^+ :

$$A^+ = A'_0 \left(1 - \frac{1}{1 + \frac{\langle \int \dot{\eta} \rangle}{5.5 \cdot 10^{-6} \cdot f_c^{2.5}}} \right) \quad (20)$$

where A'_0 is the upper limit of A in the post-transition regime, and $\langle \int \dot{\eta} \rangle$ is used to guarantee that numerically this phenomenon is only considered for passively-confined concrete as experimentally observed, while for actively-confined concrete this phenomenon is numerically suppressed.

This is demonstrated schematically in Fig. 16b showing the variation of confinement measure in the post-transition regime. For actively-confined concrete, η reaches the maximum value at the transition stage because the loading stress reaches the maximum and the confining stresses are constant. Therefore, in the post-transition regime, the confinement measure decreases and $\langle \int \dot{\eta} \rangle = 0$ and $A^+ = 0$. By contrast, for passively-confined concrete, η reaches a relatively small value at the transition stage but increases substantially in the post-transition regime, and therefore $\langle \int \dot{\eta} \rangle > 0$ and $A^+ > 0$.



The upper limit A'_0 corresponds to ψ under very high passive confinement, which has been shown in Piscesa et al. [45] to be $\nu < \psi < 0.5$. Since A_0 corresponds to $\psi_0 = \nu$, and physically it is unlikely that in the post-transition regime concrete with coalesced macro-cracks behaves in an intact state even with a very high level of passive confinement, the value of $A'_0 < A_0$ should hold. Meanwhile, since plastic volumetric compaction can be achieved under high passive confinement, $A'_0 > A_k$ should also hold. Therefore, it is reasonable to have $A'_0 = a_0 A_0 + (1 - a_0) \cdot A_k$, where

$0 \leq a_0 \leq 1$. The value of a_0 was examined against the dilation models proposed in Jiang and Teng [16] and Lim and Ozbakkaloglu [70]; a representative comparison is shown in Fig. 16c. It is seen that $a_0 = 1$ obviously over-predicts the dilation decrease while a value of $a_0 = 0$ under-predicts that; a value of $a_0 = 0.5$ agrees well with the well-established dilation models.

By combining Eq. (16) for A^- and Eq. (20) for A^+ , the evolution of the potential-surface volumetric component in the post-transition regime can be represented by the following evolution:

$$A = \max(A^-, A^+), \kappa \geq \kappa_c \quad (21)$$

As discussed in the above paragraph, Eq. (21) ensures that the post-transition dilation behavior of unconfined and actively-confined concrete is governed by A^- since $A^- > A^+ = 0$; and that of passively-confined concrete is governed by A^- initially when $A^+ < A^-$, and later governed by A^+ after the inflection point. Finally, the vertex of the potential surface on the positive hydrostatic axis remains unchanged during the pre-transition regime (see Fig. 8a), while, during the post-transition regime, it shifts along the negative hydrostatic axis direction (see Fig. 8b) as proposed by Pietruszczak et al. [54] for use in their plasticity model and subsequently adopted by Farahmandpour et al. [46] in a plasticity-based model that can closely simulate the plastic volumetric behavior of concrete. This evolution can be mathematically expressed as $B = B_0 \cdot$

$$\sqrt{c(\kappa)}, \text{ where } B_0 = \sqrt{3}/m_0, m_0 = 3 \frac{f_c^2 - f_t^2}{f_c \cdot f_t} \cdot \frac{e}{e+1}.$$

3.4 Potential-surface deviatoric parameters

The deviatoric trace of the potential surface in the present model is controlled by $\varrho(\kappa)$. Since it does not influence the concrete behavior under uniform confinement, its evolution is examined

based on the experimental data of the concrete multiaxial compression tests conducted by Mohammadi and Wu [39] and Mohammadi et al. [37]; such experimental data are rather limited. In these studies, concrete cubes were subjected to compressive loading along σ_3 and at the same time were constrained by passive confining stresses of different magnitudes along σ_1 and σ_2 , with $0 \geq \sigma_1 \geq \sigma_2 > \sigma_3$. Therefore, the plastic strains should satisfy $\varepsilon_p^1 \geq \varepsilon_p^2$. In Fig. 17, the values of $\varepsilon_p^1/\varepsilon_p^2$ extracted from the experimental data are shown against the normalized stress ($-\sigma_3/f_c^*$). Overall, they are categorized into the under-confined and the well-confined groups. In the former, $-\sigma_3$ decreases in the post-transition regime, while in the latter, it increases. Due to the large scatter and the limited amount of the data, a bootstrap-resampling method [88,89] was used to generate 1000 curves of the mean values for each group to facilitate data interpretation; the under-confined group is represented by blue curves, and the well-confined, orange curves. The median of each group of 1000 curves is highlighted as the thick white curve representing the overall trend of the group.

In the pre-transition regime, it is seen that the median curves of $\varepsilon_p^1/\varepsilon_p^2$ are quite similar for the two groups and are generally between 1.0 and 1.5 (Fig. 17). This indicates a relatively large and steady value of ϱ in the pre-transition regime, which can be interpreted as $\varrho = \varrho_0$ for $\kappa \leq \kappa_c$. In the post-transition regime, for the under-confined (blue) group, the value of $\varepsilon_p^1/\varepsilon_p^2$ increases rapidly, implying that ϱ changes rapidly from ϱ_0 to ϱ_∞ (see Section 2.3 and Fig. 9c for details), whereas for the well-confined (orange) group, it increases slowly, and hence ϱ changes slowly. As a result, the evolution of ϱ may be related to the decohesion process, i.e., the decrease of $c(\kappa)$, which is much more rapid for under-confined cases than for well-confined cases. Microscopically, the de-cohesion (softening) process results from the coalescence of microcracks into macrocracks,

which significantly promotes the (plastic/inelastic) dilation differences between the high and the low levels of confinement.

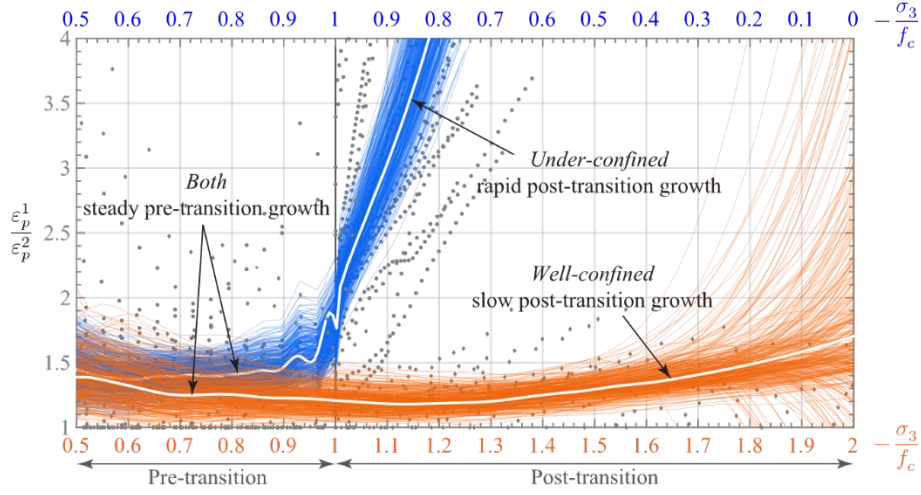


Fig.17 Differences between ε_p^1 and ε_p^2 for non-uniformly confined concrete

The correlation between c and ϱ is schematically shown in Fig. 18a, where the typical softening curves of well-confined and under-confined concretes are compared. For the well-confined concrete, the decrease of c in the post-transition regime is relatively slow which corresponds to the slow lateral dilation differentiation in Fig. 17; for the under-confined concrete, c decreases drastically upon the entrance into the post-transition regime, corresponding to the rapid lateral dilation differentiation of the under-confined concrete in Fig. 17. Therefore, it is clear that the decohesion process correlates with the potential-surface deviatoric shape as indicated in Fig. 18a. The full cohesion ($c = 1$) condition corresponds to the initial deviatoric shape (ϱ_0), and ($c \rightarrow 0$), to the final shape (ϱ_∞). It is thus proposed that the deviatoric shape of the potential surface be dictated by the following evolution process:

$$\varrho(\kappa) = \varrho_\infty + c(\kappa)^n(\varrho_0 - \varrho_\infty) \quad (22)$$

where n controls the rate of evolution, as indicated in Fig. 18b.

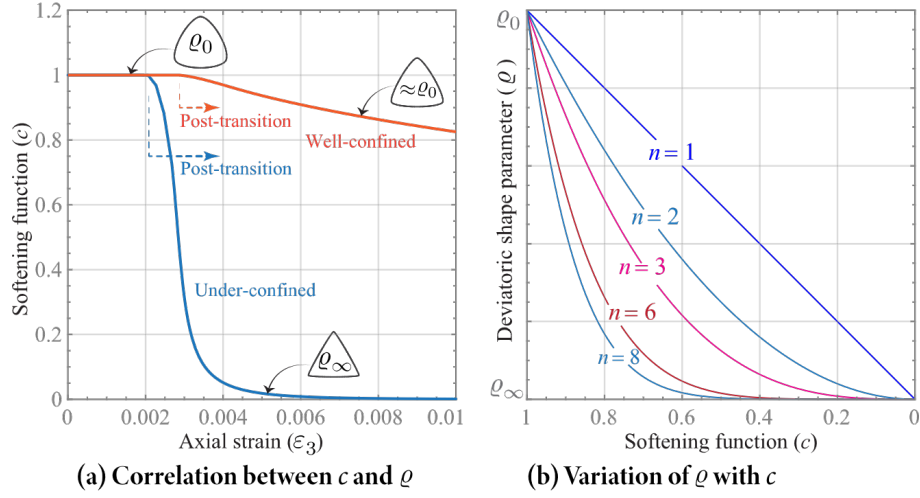


Fig.18 Relationship between potential-surface deviatoric parameter and softening function

The influence of ρ_0 , ρ_∞ , and n is illustrated by a parametric simulation example of concrete under non-uniform confinement: a concrete cube of $f_c = 40$ MPa is under compression while being passively confined with: (a) $-\sigma_1/\varepsilon_1 = 500$ MPa and $-\sigma_2/\varepsilon_2 = 1000$ MPa (well-confined case), and (b) $-\sigma_1/\varepsilon_1 = 0$ and $-\sigma_2/\varepsilon_2 = 1000$ MPa (under-confined case), respectively. Fig. 19a shows the influence of ρ_0 and ρ_∞ . For the well-confined case, the curves between the axial stress and the three principal strains are shown for values of $\rho_0 = 0.7, 0.8, \text{ and } 1.0$ (circular trace). It is seen that the circular deviatoric potential trace gives the smallest strain difference between the two lateral directions (as indicated by the black curves), while smaller values of ρ_0 lead to larger differences between ε_1 and ε_2 (as indicated by the blue and red curves). For the under-confined case, the curves between the axial stress and the three principal strains are shown for $\rho_\infty = 0.57, 0.8, \text{ and } 1.0$ (circular trace). While the influence on the dilation in the unconfined σ_1 direction is trivial, the dilation in the confined σ_2 direction is substantially influenced. The circular deviatoric trace leads to only a small difference between ε_1 and ε_2 as discussed above. Consequently, even

in this case where direction σ_1 is not confined while direction σ_2 is highly confined, the difference between ε_1 and ε_2 in the post-transition regime is still small (see the black solid and dashed curves). A nearly triangular deviatoric trace ($\varrho_\infty = 0.57$), however, leads to a large difference between ε_1 and ε_2 when the confinement is highly non-uniform. As a result, the predicted ε_2 almost vanishes in the post-transition regime (see the red curve). The influence of n is shown in Fig. 19b for both the under- and well-confined cases. It is seen that when n is smaller than 3, the predicted lateral dilation difference for the under-confined case becomes insufficient, while when n is larger than 6, the predicted lateral dilation difference for the well-confined case becomes too significant. Accordingly, in the present model, the values of $\varrho_0 = 0.85$, $\varrho_\infty = 0.57$ and $n = 3$ are used and validated against experimental data in Section 5.3.

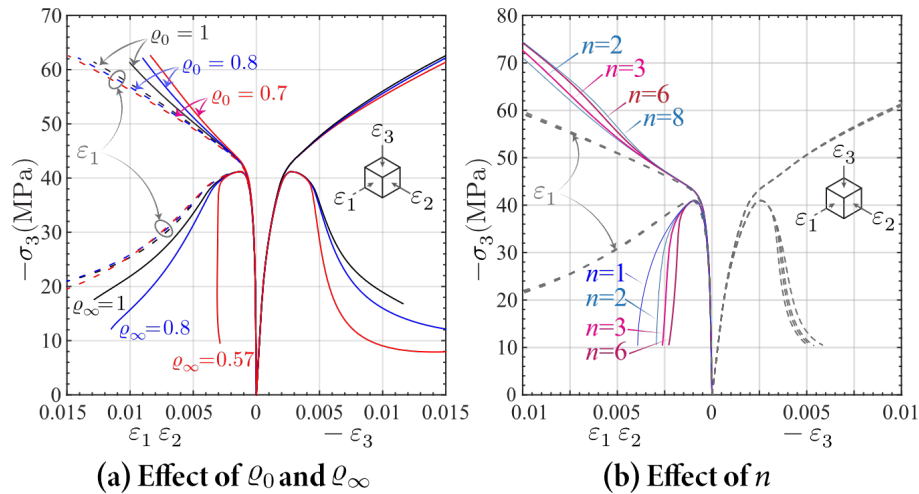


Fig.19 Effect of potential-surface deviatoric trace on stress-strain curves

3.5 Hardening/softening parameters

The ductility measure (χ_p) reflects the influence of confinement on ductility by decreasing the accumulation of the ISV with the increase of confinement. Therefore, it is a function of the confinement measure (η) as suggested in Etse and Willam [56] and Grassl and Jirásek [59]. The concrete ductility increase due to confinement has been experimentally investigated by Teng et al. [15] and Lim and Ozbakkaloglu [90] based on extensive data and expressed as the relationship between the strain in the loading direction at the transition state ($\varepsilon^{k,*}$) and the uniform confining pressure (σ_l) as follows:

$$\frac{\varepsilon^{k,*}}{\varepsilon^k} = 1 - K \frac{\sigma_l}{f_c} \quad (23)$$

where $K = 17.5$ is suggested in Teng et al. [15] and $K = 17.9$ in Lim and Ozbakkaloglu [90]. By substituting $\varepsilon^{k,*}/\varepsilon^k$ with χ_p and σ_l with η , the relationship between the ductility measure χ_p and the invariant confinement measure η is numerically obtained as follows (see Appendix E for details):

$$\chi_p = 1 + (26.3 + 0.437f_c - 0.00075f_c^2)\eta - (18.8 + 0.0975f_c)\eta^2 + 8\eta^3 \quad (24)$$

The value of κ_c is taken as the unscaled accumulated plastic strain at the transition state under uniaxial compression:

$$\kappa_c = \|\boldsymbol{\varepsilon}_p^k\| = \sqrt{\varepsilon_p^{k,1^2} + \varepsilon_p^{k,2^2} + \varepsilon_p^{k,3^2}} \quad (25)$$

where $\varepsilon_p^{k,3} = \varepsilon^k - \varepsilon_e^k$ is the plastic strain along the loading direction, and $\varepsilon_p^{k,1} = \varepsilon_p^{k,2}$ are the plastic strains perpendicular to the loading direction at the transition stress. Based on the linear evolution assumption of ψ , $\varepsilon_p^{k,1} = (\psi_0 + \psi_k)/2 \cdot \varepsilon_p^{k,3}$. Therefore, the critical plastic strain length is:

$$\kappa_c = \sqrt{(\psi_0 + \psi_k)^2/2 + 1} \cdot (\varepsilon^k - f_c/E) \quad (26)$$

The softening coefficient κ_s controls the descending branch in the post-transition regime, which is much more scattered than the ascending branch in the reported data. Therefore, the value of κ_s can be calibrated against the experimental data on a trial-and-error basis for the specific batch of concrete used in the experiments (i.e., target-calibrated). In case of unavailable experimental data, a value of $\kappa_s = 4\sim 8\kappa_c$ provides a reasonable prediction of the descending branch of the stress-strain relationship for concrete of various f_c under uniaxial compression.

4. Implementation in implicit finite element analysis

Various plasticity-based constitutive models have been implemented in FE codes to conduct nonlinear 3D analysis of concrete members, with the more representative ones being: (1) the model developed by Lee and Fenves [26] and Lubliner et al. [55] had been built into the FE package ABAQUS [35], which has been employed in many studies (e.g., [37,71]); (2) the pressure-sensitive plastic-damage model developed by Červenka and Papanikolaou [58] was implemented in ATENA [91] to analyze a beam with mild-steel longitudinal reinforcement and a column with longitudinal and transverse mild-steel reinforcement; (3) the model developed by Abu Al-Rub and Kim [92] was implemented in ABAQUS through the user-defined material (UMAT) subroutine for the fracture analysis of concrete under tension; (4) the model developed by Grassl et al. [72] was implemented in OOFEM [93] for the analysis of a plain concrete beam and a plain concrete column; (5) the model modified from Papanikolaou and Kappos [28] by incorporating the dilation behavior of concrete with uniform FRP confinement [45] was implemented in a customized FE code [57] to analyze circular-section concrete columns confined with an external FRP jacket and internal mild-steel spirals.

The proposed plasticity constitutive model has been implemented in the general-purpose FE package ABAQUS [35] through the user-defined material (UMAT) subroutine. The general structure of implicit integration has been elaborated in many previous studies (e.g., [27,28]) and therefore is not herein repeated. However, since the present model adopts a θ -dependent potential surface, some modifications have been made to improve the convergence performance, and these modifications are explained as follows.

For the $(n + 1)^{th}$ implicit incremental step, the initial stress ($\boldsymbol{\sigma}^n$), state-dependent variables (\mathbf{s}^n), elastic stiffness (D), and strain increment ($\boldsymbol{\varepsilon}$) are given. A trial stress is obtained as $\boldsymbol{\sigma}^{tr} = \boldsymbol{\sigma}^n + D\boldsymbol{\varepsilon}$, and if it is within the current yield surface ($f(\boldsymbol{\sigma}^{tr}; \mathbf{s}^n) < 0$), it is a linear-elastic step. Otherwise, an initial stress return is executed by finding the plastic strain length $\dot{\lambda}^{(0)}$ that fulfills $f(\boldsymbol{\sigma}^{tr} - \dot{\lambda}^{(0)} \cdot D \cdot \mathbf{g}_\sigma(\boldsymbol{\sigma}^{tr}; \mathbf{s}^n); \mathbf{s}^n) = 0$, where \mathbf{g}_σ denotes the return direction as determined by the plastic potential function. Subsequently, different from the previous models assigning $\boldsymbol{\sigma}^{(0)} = \boldsymbol{\sigma}^{tr} - \dot{\lambda}^{(0)} \cdot D \cdot \mathbf{g}_\sigma(\boldsymbol{\sigma}^{tr}; \mathbf{s}^n)$, only $\dot{\lambda}^{(0)}$ is preserved while another implicit step is taken to find the *consistent return direction* that meets $\boldsymbol{\sigma}^{(0)} = \boldsymbol{\sigma}^{tr} - \dot{\lambda}^{(0)} \cdot D \cdot \mathbf{g}_\sigma(\boldsymbol{\sigma}^{(0)}; \mathbf{s}^{(0)})$. A schematic of the consistent initial return is shown in Fig. 20a, where it shows that the return direction $\mathbf{g}_\sigma(\boldsymbol{\sigma}^{(0)}; \mathbf{s}^{(0)})$ is consistent with the current stress $\boldsymbol{\sigma}^{(0)}$ and state-dependent variables $\mathbf{s}^{(0)}$. This step substantially improves the convergence performance as otherwise the mismatch between $\mathbf{g}_\sigma(\boldsymbol{\sigma}^{tr}; \mathbf{s}^n)$ and $\mathbf{g}_\sigma(\boldsymbol{\sigma}^{(0)}; \mathbf{s}^{(0)})$ may cause numerical instability for non-uniform stress states where θ substantially influences the return direction. Thereafter, the regula-falsi iteration is used to allow the convergence of $f(\boldsymbol{\sigma}^{tr} - \dot{\lambda}^{(i)} \cdot D \cdot \mathbf{g}_\sigma(\boldsymbol{\sigma}^{(i)}; \mathbf{s}^{(i)}); \mathbf{s}^{(i)})$ to zero within a pre-set tolerance (typically of the order of $10^{-3}\dot{\lambda}$). In each iteration, the consistent return direction is also

used, as shown in Fig. 20b. Upon meeting the tolerance, the stress, strain, and state-dependent variables are updated accordingly.

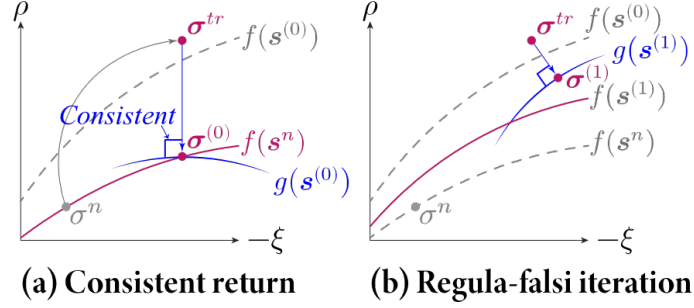


Fig.20 Schematic of iterative determination process of stress state

The consistent tangent stiffness [94] is not used due to the complicated explicit form of $g_{\sigma\sigma}$. Instead, the continuum tangent stiffness (D^{ep}) as follows is used:

$$D^{ep} = \frac{\dot{\sigma}}{\dot{\epsilon}} = D - \frac{Dg_{\sigma}f_{\sigma}^T D}{f_{\sigma}^T Dg_{\sigma} - f_{\sigma}^T f_{\kappa}} \quad (27)$$

where $f_{\sigma} = f_{\rho} \cdot \rho_{\sigma} + f_{\xi} \cdot \xi_{\sigma} + f_{\theta} \cdot \theta_{\sigma}$, and $g_{\sigma} = g_{\rho} \cdot \rho_{\sigma} + g_{\xi} \cdot \xi_{\sigma} + g_{\theta} \cdot \theta_{\sigma}$. For uniform confinement, it has $\theta = 60^{\circ}$, and both can be simplified by $f_{\theta} = 0$ and $g_{\theta} = 0$. It is noted that the convergence rate achievable with the continuum tangent stiffness is inferior to that achievable with the consistent tangent stiffness. Nevertheless, the continuum tangent stiffness approach still provides acceptable convergence performance and computation time [28,95].

5. Numerical evaluation

Given the scope of the present paper, the proposed plasticity constitutive model is evaluated herein at the material level (represented by a cube under uniform pressure in all three directions). Therefore, an FE model containing a single 8-node brick element with reduced integration of 10

mm in side length was built with ABAQUS to predict the mechanical behavior of concrete under monotonic compression with no confinement, uniform active confinement, uniform passive confinement, and non-uniform passive confinement. The results are compared with experimental data reported by other researchers in the open literature to evaluate the performance of the proposed constitutive model. More specifically, to demonstrate that the proposed model works well for both actively- and passively-confined concrete, the test data reported by Lim and Ozbakkaloglu [17] were selected for comparison because the same batch of concrete was used in their study to fabricate specimens for both active- and passive-confinement tests. Therefore, identical material parameters were used for the predictions presented in Section 5.1 (active confinement cases) and 5.2 (passive confinement cases). To demonstrate the capability of the model in predicting the behavior of concrete under non-uniform passive confinement, the experimental data reported by Mohammadi and Wu [39] were selected for comparison, as there have been few such studies and the tests conducted by Mohammadi and Wu [39] covered the widest range of non-uniform confinement scenarios within a single study. Additionally, the model was used to simulate the tests conducted by Jiang et al. [96], and close predictions were achieved, which are however not reported herein for brevity.

5.1 Concrete under uniform active confinement

The single-element FE model was used to simulate the compression tests of circular concrete cylinders under different levels of active confinement reported by Lim and Ozbakkaloglu [17], where a Hoek cell was used to apply hydraulic confining pressure to a circular concrete cylinder. The active confinement was simulated in the FE model by applying a constant pressure ($\sigma_1 = \sigma_2$)

in the two directions perpendicular to the axial compression (σ_3). The uniaxial compressive strength (f_c) obtained from a single compression test on an unconfined circular concrete cylinder of 63 mm in diameter and 126 mm in height was directly used for making the predictions since the confined circular concrete cylinder specimens had the same dimensions; the axial strain (ε^k) used in the numerical simulations was also taken directly from the corresponding axial stress-strain curve while the elastic modulus (E) was calculated from the same curve according to ASTM C469 [97]. In addition, the value of the softening rate parameter (κ_s) was determined by matching the predicted descending branch of the axial stress-strain curve with the experimental axial stress-strain curve. An approximate Poisson's ratio (ν) was found from the axial strain-lateral strain curve of the same unconfined cylinder specimen, while the plastic Poisson's ratio at the transition state (ψ_k) was calculated using Eq. (14). The value of the spurious uniaxial tensile strength (\bar{f}_t), used in a convenient approach for adjusting the friction angle, was determined by matching the predicted peak strength of the specimen under a given level of active confinement (e.g., 5 MPa) with the test data. The values of all parameters used in the simulations are listed in Table 2 for the four groups with different active confining stress levels.

Table 2 Model parameters for concrete tested under uniform active confinement [17]

Group	f_c [MPa]	E [MPa]	ν	ε^k	ψ_k	κ_s/κ_c	\bar{f}_t/f_c	$\sigma_1 = \sigma_2$ [MPa]
1								—
2								-5.00
3	50.0	36000	0.2	-0.0022	0.8	8	0.10	-10.00
4								-15.0
5								-25.0

The predicted axial stress-strain ($\sigma_3 - \varepsilon_3$) curves and dilation behaviors ($\varepsilon_3 - \varepsilon_1$ curves) for the unconfined and actively confined concrete are shown against the experimental data in Fig. 21. Both the axial compressive strength (f_c^*) and the associated strain ($\varepsilon^{k,*}$) of the concrete are seen to increase with an increase in the confining stress. Using the calibrated values of the parameters as discussed above, the former is dictated by the adopted strength surface, and the latter by the ductility measure. The close match between the predictions and the experimental data indicates the suitability of these two components for actively confined concrete.

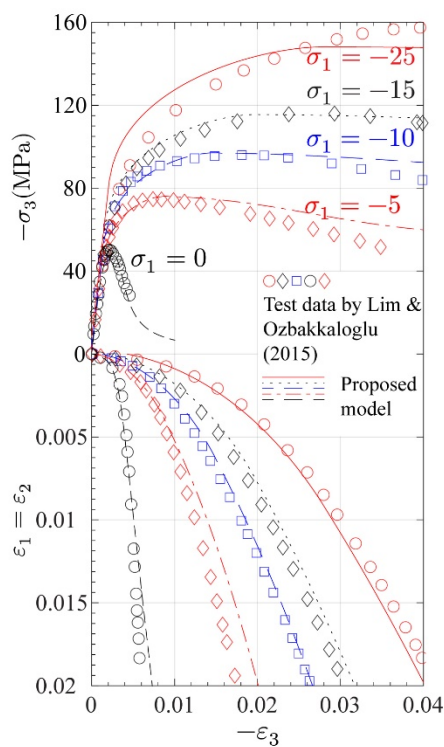


Fig.21 Predictions versus test data for concrete compression tests with uniform active confinement conducted by Lim and Ozbakkaloglu [17]

The volumetric dilation behavior of the unconfined and actively confined concrete is represented by the $\varepsilon_3 - \varepsilon_1$ curves. For the unconfined concrete, the dilation ($|\varepsilon_1|/|\varepsilon_3|$) is relatively small in the pre-transition stage while it increases rapidly in the post-transition stage as shown by the black circles, which is well predicted by the proposed constitutive model through the evolution of A^- in the potential function (see Section 3.3). For actively confined concrete, a rapid increase of dilation also occurs in the post-transition stage, while the dilation decreases with an increase in the confining stress due to the combined effect of the ductility measure and the pressure-sensitive potential function. This accurate prediction of dilation behavior indicates that the volumetric components of the proposed model are suitable for actively confined concrete.

5.2 Concrete under uniform passive confinement

Compression tests of circular concrete cylinders confined with CFRP, aramid FRP (AFRP), and glass FRP (GFRP) jackets reported in Lim and Ozbakkaloglu [17] were predicted using the proposed constitutive model. Since the specimens were subjected to uniform passive confinement, the confinement was simulated through the provision of a constant confining stiffness $\sigma_1/\varepsilon_1 = \sigma_2/\varepsilon_2$ to the single-element FE model in the two principal stress directions perpendicular to the axial compression (σ_3). A total of seven groups were simulated; the reported confining stiffness and concrete compressive strength were used, and the other parameters were determined based on the stress-strain curves of the unconfined concrete. The material parameters are identical to those used in Section 5.1 for the actively-confined concrete, as listed in Table 3.

Table 3 Model parameters for concrete tested under uniform passive confinement [17]

Group	f_c [MPa]	E [MPa]	ν	ε^k	ψ_k	κ_s/κ_c	\bar{f}_t/f_c	Confinement	$\frac{\sigma_1}{\varepsilon_1} = \frac{\sigma_2}{\varepsilon_2}$ [MPa]
1								None	0
2								CFRP, 1 layer	-830
3								CFRP, 2 layer	-1660
4	50.0	36000	0.2	-0.0022	0.8	8	0.10	AFRP, 1 layer	-810
5								AFRP, 2 layer	-1620
6								GFRP, 1 layer	-605
7								GFRP, 2 layer	-1210

The predicted $\sigma_3 - \varepsilon_3$ and $\varepsilon_3 - \varepsilon_1$ curves for all seven groups are shown against the experimental data in Fig. 22. For concrete under uniform passive confinement, in the pre-transition regime, the axial stress-strain behavior and the dilation behavior are close to those of unconfined concrete, as shown in Fig. 22a. This is because the amount of dilation is small, and hence the passive confining stress is trivial. At the beginning of the post-transition stage, the dilation increases rapidly, and the corresponding confining stress also increases rapidly. Therefore, the predicted dilation of passively confined concrete is smaller than that of unconfined concrete due to the pressure-sensitive potential surface and the ductility measure. Meanwhile, the predicted axial stress increases due to the continuous increase of the confining stress and the multiaxial strength behavior.

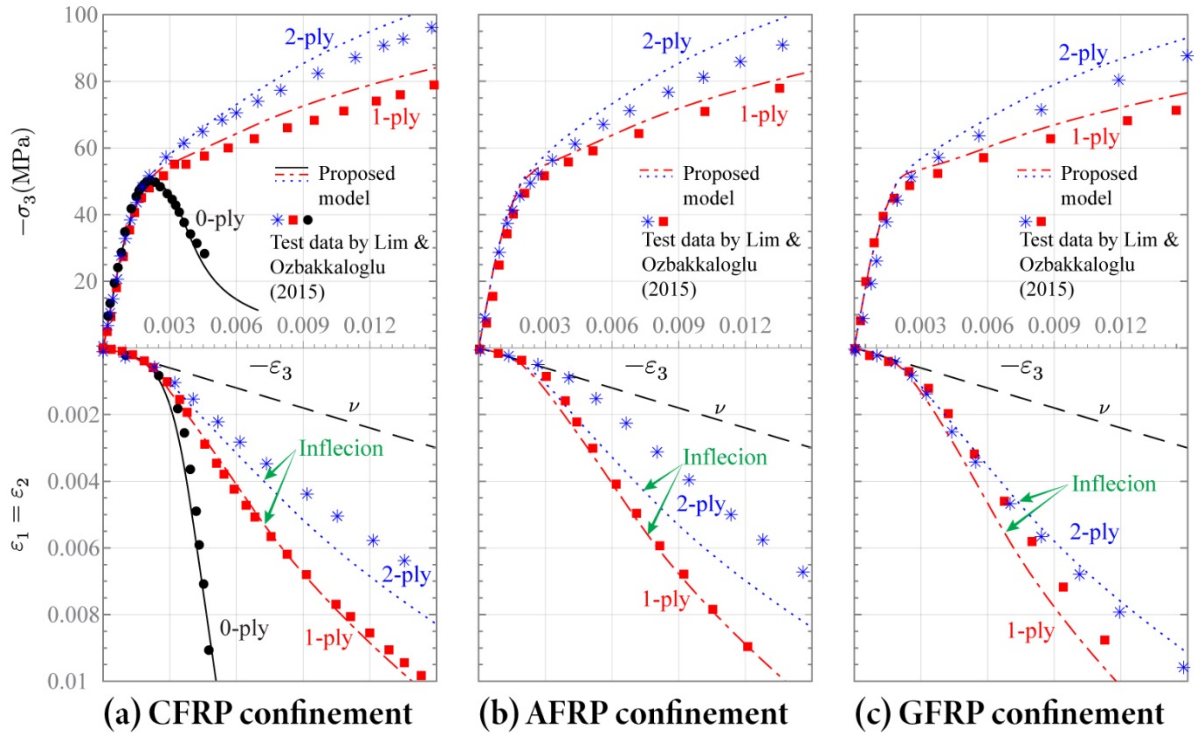


Fig.22 Predictions versus test data for concrete compression tests with uniform FRP confinement conducted by Lim and Ozbakkaloglu [17]

Thereafter, when the confining stress is large enough, an inflection point occurs on the axial-lateral strain curve, as indicated in the figure, where the rate of increment of the dilation starts to decrease. This is a unique behavior for passively confined concrete that is not seen for actively confined concrete. The accurate prediction of this behavior indicates that the A^+ parameter in the potential function is suitable for predicting the volumetric behavior of passively confined concrete. Although the increase in dilation slows down, the continuous increase of lateral dilation leads to a continuously increasing axial stress. Comparisons between the predictions and the experimental data for all the seven groups indicate that the proposed model is of good accuracy overall. The mismatch between the prediction and the 2-ply test data for GFRP-confined concrete in Fig. 22c may not be a concern as the reliability of the 2-ply test data, being almost coincidental

with the 1-ply test data, is suspicious. The proposed model is thus deemed to have successfully captured the critical features of concrete under uniform passive confinement.

5.3 Concrete under non-uniform passive confinement

The compression tests of concrete cubes under non-uniform passive confinement reported in Mohammadi and Wu [39,40] were predicted using the proposed constitutive model. In the single-element FE model, the concrete was axially compressed with σ_3 and provided with unequal confining stiffnesses $E_1 = |\sigma_1/\varepsilon_1| < E_2 = |\sigma_2/\varepsilon_2|$ in the two directions perpendicular to the axial compression. A total of nine cube specimens were simulated, with a uniaxial compressive cube strength of 28.3, 42.8, or 52.8 MPa under uniform ($0 > \sigma_1 = \sigma_2 > \sigma_3$), moderately non-uniform ($0 > \sigma_1 > \sigma_2 > \sigma_3$), and highly non-uniform ($0 = \sigma_1 \gg \sigma_2 > \sigma_3$) confining conditions, respectively. These concrete uniaxial compressive strengths [39,40] were obtained from compression tests on 150 mm concrete cubes and were directly used in the simulations since the simulated confined concrete cubes had the same dimensions. The confining stiffnesses were designed as multiples of 540 MPa and are thus normalized herein as $\bar{E} = E/540\text{MPa}$ for convenience, and the specimens are denoted by names representing their uniaxial compressive strength and confinement level in the discussions below for convenience: C28.3_0.5_2 refers to the specimen with a uniaxial compressive cube strength of 28.3 MPa and non-uniform confinement having $\bar{E}_1 = 0.5$ and $\bar{E}_2 = 2$, and C52.8_2_2 refers to the specimen with a cube strength of 52.8 MPa and uniform confinement having $\bar{E}_1 = \bar{E}_2 = 2$.

It should be noted that these authors [39,40] reported only the axial compressive strengths from tests on unconfined cube specimens but provided neither the axial stress-strain curves nor the axial stress-lateral strain curves of the cube specimens. As a result, the test results from the two concrete cube specimens under the smallest level of non-uniform confinement, i.e., $\bar{E}_1 = 0$ and $\bar{E}_2 = 0.5$, were used to determine the average elastic modulus (E) according to ASTM C469 [97] and the average axial strain at peak strength (ε^k); the value of the softening rate parameter (κ_s) was deduced by matching the predicted descending branch of the axial stress-strain curve with the test data. Since the axial strain-lateral strain curves of the unconfined cube specimen were not available, a common value for the Poisson's ratio (ν), namely 0.18, was assumed, and the default value of the plastic Poisson's ratio was adopted for the transition state ($\psi_k = 1.0$). The default values for the potential deviatoric parameters (i.e., $\varrho_0 = 0.85$ and $\varrho_\infty = 0.57$) were used. The spurious uniaxial tensile strength (\bar{f}_t) was determined by matching the predictions with the experimental data of the cube specimens under uniform passive confinement. It is noted that for specimens with the same cube strength, each of the material parameters had a constant value, as summarized in Table 4.

Table 4 Model parameters for concrete tested under non-uniform passive confinement

[39]

Specimens	f_c [MPa]	E [MPa]	ν	ε^k	ψ_k	κ_s/κ_c	\bar{f}_t/f_c	$\frac{\sigma_1}{\varepsilon_1}$ [MPa]	$\frac{\sigma_2}{\varepsilon_2}$ [MPa]
C28.3_0_2	28.3	30000	0.18	-0.0028	1.0	6	0.12	0	-1080
C28.3_1_1								-540	-540

C28.3_0.5_2								-270	-1080
C42.8_0.5_0.5								-270	-270
C42.8_0.5_2	42.8	34000	0.18	-0.0026	1.0	6	0.12	-270	-1080
C42.8_0_2								0	-1080
C52.8_2_2								-1080	-1080
C52.8_1_2	52.8	36200	0.18	-0.0025	1.0	6	0.12	-540	-1080
C52.8_0_2								0	-1080

The predictions and experimental data of the stress in the loading direction ($-\sigma_3$) and strains in the three principal directions ($\varepsilon_1, \varepsilon_2, -\varepsilon_3$) are compared in Figs. 23-25. Fig. 23 shows comparisons for concrete cube specimens C28.3_1_1, C42.8_0.5_0.5 and C52.8_2_2, which were under uniform confinement and thus had identical strains in the two lateral directions. The well-confined specimens C28.3_1_1 and C52.8_2_2 exhibit strain-hardening in the post-transition regime, but the under-confined case C42.8_0.5_0.5 exhibits a plateau in the post-transition regime. Both cases are well predicted by the proposed model.

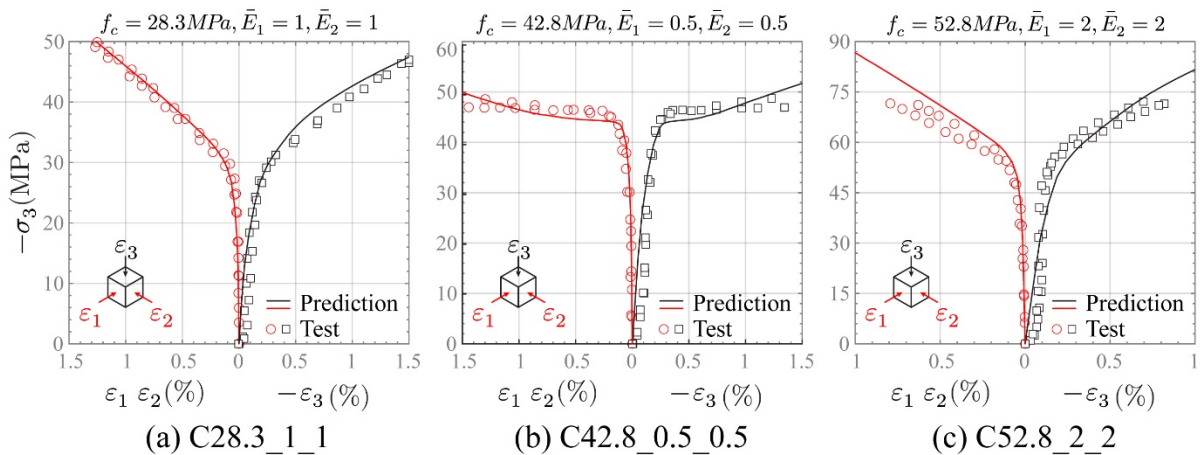


Fig.23 Predictions versus test data for compression tests of concrete cubes conducted by Mohammadi and Wu [39]: uniform passive confinement

Fig. 24 shows comparisons for concrete cube specimens C28.3_0.5_2, C42.8_0.5_2 and C52.8_1_2, which were under moderately non-uniform passive confinement. The specimens exhibit strain-hardening in the post-transition regime, and the differences between ε_1 and ε_2 are moderate. By comparing the results of C52.8_2_2 and C52.8_1_2, it is seen that reducing \bar{E}_1 by half has a limited influence on the behavior. For this confining condition, the deviatoric dilation behavior is mainly dependent on ϱ_0 as the decohesion process is slow due to the ductility measure. The close match between the predictions and experimental data for all three groups in Fig. 24 indicates that the proposed deviatoric trace of the potential surface is suitable for concrete under moderately non-uniform confinement. It is noticed that since decohesion is moderate, the deviatoric trace is still more circular than triangular. Moreover, the unequal confining stresses are not too different, so that θ is close to 60° .

To further evaluate the performance of the proposed model, specimen C28.3_0.5_2 was simulated in the present study using the AA damage-plasticity model proposed by Yu et al. [38] (referred to as AA1 in the discussions below). The values of uniaxial compressive strength, elastic modulus, and the corresponding axial strain used in the simulation were 28.3 MPa, 30000 MPa, and 0.0028, respectively; default values generated by AA1 were used for the other parameters. The predicted results are compared with those of the proposed model in Figure 24. Moreover, the authors who conducted the tests also simulated specimen C42.8_0.5_2 using an AA Linear D-P plasticity model [37] (referred to as AA2 in the discussions below) modified from [34], and simulated specimen C52.8_1_2 using an AA damage-plasticity model [39] (referred to as AA3 in the discussions below) modified from [38]. The values of uniaxial compressive strength used

in the simulations were 42.8 and 52.8 MPa respectively, and the details of the other parameters used in the simulations can be found in [37,39]. The simulation results obtained by these authors were extracted from figures in [37,39] and are compared with the predictions of the proposed model in Figure 24. AA1 and AA3 employ a circular and thus θ -independent potential-surface deviatoric trace as mentioned earlier, while AA2 employs a θ -dependent non-circular potential-surface deviatoric trace that is associative with the yield-surface deviatoric trace as explained in detail in [35]. It is seen in Figure 24 that the predictions of the AA plasticity models are generally close to those of the proposed model, and this is because, for moderately non-uniform confinement, the difference between the lateral dilations is still moderate and hence can be well approximated by a circular or associative potential-surface deviatoric trace. Similarly, it is expected that the trefoil potential-surface deviatoric trace [28] is of acceptable accuracy for concrete under moderately non-uniform confinement.

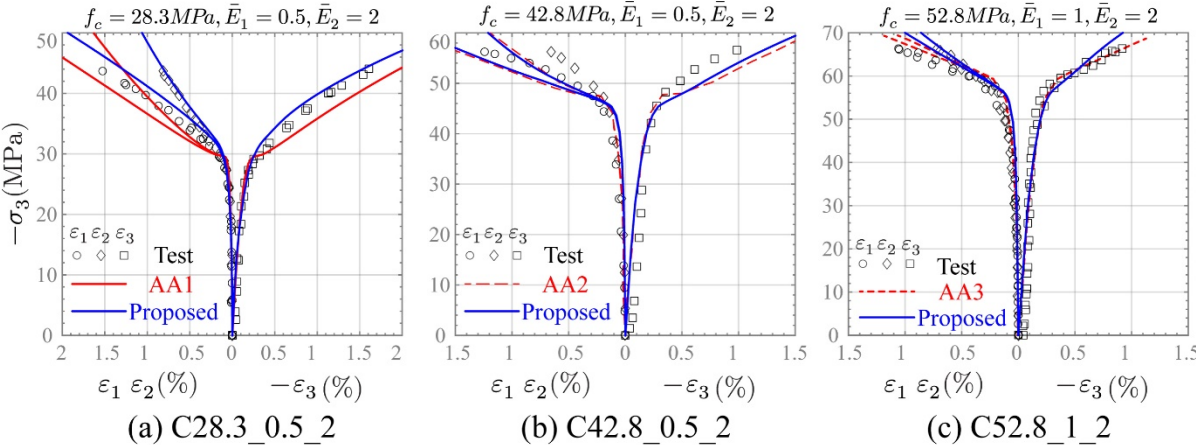


Fig.24 Predictions versus test data for compression tests of concrete cubes conducted by Mohammadi and Wu [39]: moderately non-uniform passive confinement

For specimens C28.3_0_2, C42.8_0_2, and C52.8_0_2 which are under highly non-uniform passive confinement, as shown in Fig. 25, the behavior is akin to that of the under-confined concrete: a slightly increased transition stress and a post-transition descending branch. Even with a high level of confinement in the σ_2 direction, the absence of confinement in the σ_1 direction results in nearly no confinement effect. By comparing the results of specimens C52.8_2_2, C52.8_1_2, and C52.8_0_2, it is seen that reducing the confining stiffness in the σ_1 direction to zero has a significant influence on the behavior.

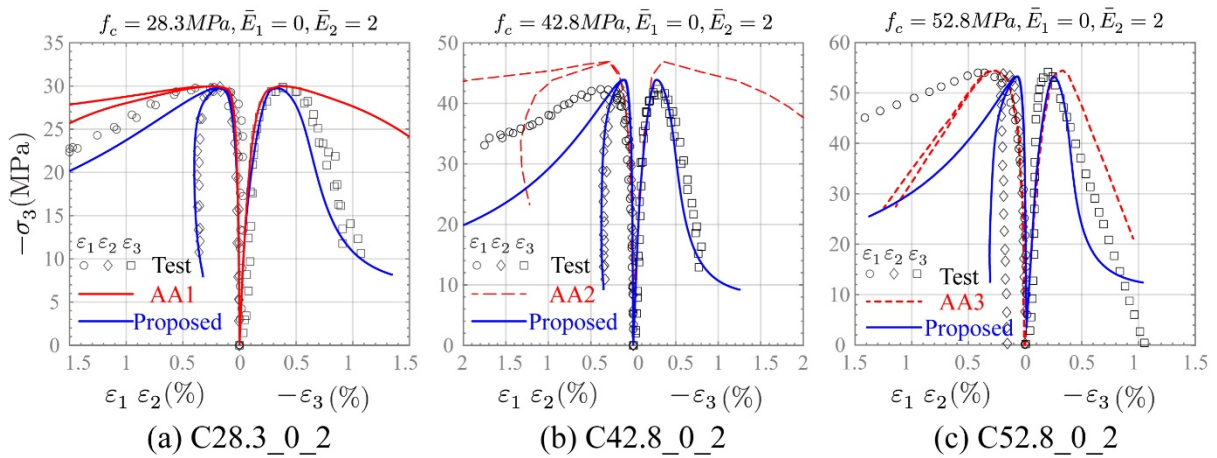


Fig.25 Predictions versus test data for compression tests of concrete cubes conducted by Mohammadi and Wu [39]: highly non-uniform passive confinement

A very large amount of dilation is seen in the unconfined σ_1 direction (red curves), while in the confined σ_2 direction (blue curves), the strain hardly increases in the post-transition regime. The proposed model accurately captures this dramatic deformational behavior, indicating that the proposed deviatoric trace of the potential surface is suitable for concrete under severely non-uniform confinement. Specifically, the deviatoric component of the potential surface evolves

quickly into a state with a small value of ρ_∞ in the post-transition stage due to rapid decohesion. As a result, the nearly triangular deviatoric trace predicts a large difference between ε_1 and ε_2 .

Similarly, specimen C28.3_0_2 was simulated in the present study using AA1 with the uniaxial compressive strength, the corresponding axial strain, and the elastic modulus being 28.3 MPa, 30000 MPa, and 0.0028, respectively; default values generated by AA1 were used for the other parameters. The predicted results are compared with those of the proposed model in Figure 25. Specimens C42.8_0_2 and C52.8_0_2 were simulated by the authors who conducted the tests using AA2 and AA3 with the uniaxial compressive strengths being 42.8 and 52.8 MPa, respectively; details of the other parameters used in the simulations can be found in [37,39]. Their simulation results were extracted from figures in [37,39] and are compared with those of the proposed model in Figure 25. As mentioned earlier, the θ -independent circular potential-surface deviatoric trace is incapable of predicting a large difference between the lateral plastic dilations (Fig. 19a). This can be seen in Figure 25 where the differences between ε_1 and ε_2 predicted by AA1 and AA3 are much smaller than those predicted by the proposed model. Therefore, a potential surface with a circular deviatoric trace is inaccurate in predicting the dilation behavior of concrete under highly non-uniform confinement. Furthermore, although AA2 employs a θ -dependent non-circular potential-surface deviatoric trace and hence predicts a relatively large difference between ε_1 and ε_2 as seen in the figure, the deviatoric trace is fixed to be identical in shape to the yield surface (associativity) [35]. Therefore, its dilation predictions are still much less accurate than those of the proposed model which employs a potential surface with an evolution rule interpreted from experimental data.

The accurate prediction of deformation behavior of concrete under highly non-uniform confinement has major implications for the structural analysis of non-uniformly confined concrete members. It is seen that the dilations predicted by the proposed model and the AA plasticity models can be very different. If the dilation behavior is not accurately captured, the predicted stress behavior of a confined concrete member is likely to be inaccurate. More specifically, the predicted dilation behavior of the concrete influences its interaction with the neighboring materials, which, in turn, influences the predicted behavior of the structural member. Therefore, the proposed constitutive model is superior to the AA plasticity models for predicting the nonlinear behavior of structural members containing concrete that is under non-uniform (passive) confinement.

6. Concluding remarks

Concrete structural members, especially when designed to mainly resist axial compression, are often laterally confined to achieve superior performance in both strength and ductility. The structural behavior of such members involves complex interactions between the dilating concrete and the confining material(s). While this dilation-confinement interaction is relatively simple for concrete under uniform confinement, which is only found in concentrically loaded circular-section members, it is substantially more complicated for non-uniform confinement scenarios, which are commonly found in members involving eccentric loading, non-circular sections, and multiple confining materials. The accurate prediction of the structural behavior of confined concrete members requires the use of an accurate 3D constitutive model which is normally based on the theory of plasticity. However, existing plasticity constitutive models are inadequate in a

number of aspects, including theoretical rigor and predictive accuracy, especially when the concrete is under non-uniform passive confinement.

A 3D plasticity constitutive model that can accurately predict the behavior of concrete under various confining conditions has been proposed in the present paper for the analysis of confined concrete members. The components of the model were formulated based on the following experimental observations of concrete under compression with active uniform confinement, passive uniform confinement, and passive non-uniform confinement:

- i. Experimental observations have indicated that the multiaxial compressive strength of concrete is nearly path-independent. The widely adopted Menetrey-Willam strength surface has been proven appropriate by previous researchers and is employed in the proposed model.
- ii. For structural members with confined concrete, the confining stress is activated by the lateral dilation of concrete. The axial compressive stress is dominant in magnitude so that the stress path is very unlikely to intersect the cap of a yield surface. Therefore, straightforward, open yield surfaces have been employed in the proposed model.
- iii. Regarding volumetric dilation behavior, confined concrete exhibits hydrostatic pressure-dependent dilation behavior. Moreover, both plastic volumetric compaction and dilation have been experimentally observed for confined concrete. To capture both phenomena, capped meridians for the potential surface featuring smooth pressure-dependent transition of plastic volumetric dilation to compaction have been employed in the proposed model.

- iv. The experimental research on concrete under non-uniform passive confinement, though somewhat limited, has revealed its unique deviatoric dilation behavior. Bulged-triangular deviatoric potential traces featuring an adjustable and convex shape allow the prediction of a diverse range of deviatoric dilation behavior and have thus been employed in the proposed model and calibrated with the available experimental data.
- v. The internal state variable has been defined as the total plastic strain length factored by a ductility measure. As a result, the total plastic strain length is compatible with the plastic volumetric compaction capability, and pressure-dependent ductility is well depicted by the proposed ductility measure.

The proposed constitutive model has been numerically calibrated against extensive experimental data to internalize the concrete behavior under various confining conditions. The implementation of the model in implicit finite element analysis through the general-purpose FE package ABAQUS with an enhanced stress-return algorithm suitable for the novel potential surface has also been explained. The performance of the proposed constitutive model has been evaluated through simulating the mechanical response of concrete under uniform active, uniform passive, and non-uniform passive confining conditions. The comparisons between the predictions and experimental data indicate that the model is successful in capturing the key features and highly adjustable for various confining conditions to achieve accurate predictions upon targeted calibration.

The proposed model as described in the present paper is limited to compression-dominant stress conditions and monotonic loading, but it can be readily combined with damage/fracture theories

(e.g., [29,58,72]) to cover both compression-dominated and tension-dominated stress conditions. For certain finite element applications, it is also subject to mesh dependence, which however can be addressed using nonlocal averaging algorithms (e.g., [98–100]).

Acknowledgment

The authors are grateful for the financial support received from the Research Grants Council (RGC) of the Hong Kong Special Administrative Region, China, through a Theme-based Research Scheme (Project No.: T22-502/18-R) and a National Natural Science Foundation of China (NSFC)/RGC Joint Research Scheme (Project No.: N_PolyU520/16). The authors wish to thank their research group members, Mr. Kaicheng Liu, Dr. Zheng Huang and Dr. Guan Lin, for their valuable comments on an earlier version of the manuscript.

References

- [1] Imran I, Pantazopoulou SJ. Experimental study of plain concrete under triaxial stress. *ACI Mater J* 1996;93:589–601. <https://doi.org/10.14359/9865>.
- [2] Kupfer H, Hilsdorf HK, Rusch H. Behavior of concrete under biaxial stresses. *ACI J Proc* 1969;66:853–66. <https://doi.org/10.14359/7388>.
- [3] Menetrey P, Willam KJ. Triaxial failure criterion for concrete and its generalization. *ACI Struct J* 1995;92:311–8. <https://doi.org/10.14359/1132>.
- [4] Willam KJ, Warnke EP. Constitutive model for the triaxial behaviour of concrete. *Concr. Struct. Subj. to Triaxial Stress.*, Zurich: International Association of Bridge and Structural Engineers; 1974, p. 1–30.

- [5] Sheikh SA, Uzumeri SM. Strength and ductility of tied concrete columns. *J Struct Div* 1980;106:1079–102. <https://doi.org/10.1061/JSDEAG.0005416>.
- [6] Mander JB, Priestley MJN, Park R. Observed stress-strain behavior of confined concrete. *J Struct Eng* 1988;114:1827–49. [https://doi.org/10.1061/\(ASCE\)0733-9445\(1988\)114:8\(1827\)](https://doi.org/10.1061/(ASCE)0733-9445(1988)114:8(1827)).
- [7] Akiyama M, Suzuki M, Frangopol DM. Stress-averaged strain model for confined high-strength concrete. *ACI Struct J* 2010;107:179–88. <https://doi.org/10.14359/51663534>.
- [8] Wei Y, Wu YF. Compression behavior of concrete columns confined by high strength steel wire. *Constr Build Mater* 2014;54:443–53. <https://doi.org/10.1016/j.conbuildmat.2013.12.083>.
- [9] Shahawy M, Mirmiran A, Beitelman T. Tests and modeling of carbon-wrapped concrete columns. *Compos Part B Eng* 2000;31:471–80. [https://doi.org/10.1016/S1359-8368\(00\)00021-4](https://doi.org/10.1016/S1359-8368(00)00021-4).
- [10] Fam A, Cole B, Mandal S. Composite tubes as an alternative to steel spirals for concrete members in bending and shear. *Constr Build Mater* 2007;21:347–55. <https://doi.org/10.1016/j.conbuildmat.2005.08.016>.
- [11] Mander JB, Priestley MJN, Park R. Theoretical stress-strain model for confined concrete. *J Struct Eng* 1988;114:1804–26. [https://doi.org/10.1061/\(ASCE\)0733-9445\(1988\)114:8\(1804\)](https://doi.org/10.1061/(ASCE)0733-9445(1988)114:8(1804)).
- [12] Lam L, Teng JG. Ultimate condition of fiber reinforced polymer-confined concrete. *J Compos Constr* 2004;8:539–48. [https://doi.org/10.1061/\(asce\)1090-0268\(2004\)8:6\(539\)](https://doi.org/10.1061/(asce)1090-0268(2004)8:6(539)).
- [13] Lam L, Teng JG. Design-oriented stress–strain model for FRP-confined concrete. *Constr Build Mater* 2003;17:471–89. [https://doi.org/10.1016/S0950-0618\(03\)00045-X](https://doi.org/10.1016/S0950-0618(03)00045-X).
- [14] Ozbakkaloglu T, Lim JC, Vincent T. FRP-confined concrete in circular sections: Review and assessment of stress–strain models. *Eng Struct* 2013;49:1068–88. <https://doi.org/10.1016/j.engstruct.2012.06.010>.

- [15] Teng JG, Huang YL, Lam L, Ye LP. Theoretical model for fiber-reinforced polymer-confined concrete. *J Compos Constr* 2007;11:201–10. [https://doi.org/10.1061/\(ASCE\)1090-0268\(2007\)11:2\(201\)](https://doi.org/10.1061/(ASCE)1090-0268(2007)11:2(201)).
- [16] Jiang T, Teng JG. Analysis-oriented stress-strain models for FRP-confined concrete. *Eng Struct* 2007;29:2968–86. <https://doi.org/10.1016/j.engstruct.2007.01.010>.
- [17] Lim JC, Ozbakkaloglu T. Investigation of the influence of the application path of confining pressure: Tests on actively confined and FRP-confined concretes. *J Struct Eng* 2015;141:04014203. [https://doi.org/10.1061/\(ASCE\)ST.1943-541X.0001177](https://doi.org/10.1061/(ASCE)ST.1943-541X.0001177).
- [18] Pantazopoulou SJ, Mills RH. Microstructural aspects of the mechanical response of plain concrete. *ACI Mater J* 1995;92:605–16. <https://doi.org/10.14359/9780>.
- [19] Candappa DC, Sanjayan JG, Setunge S. Complete triaxial stress-strain curves of high-strength concrete. *J Mater Civ Eng* 2001;13:209–15. [https://doi.org/10.1061/\(ASCE\)0899-1561\(2001\)13:3\(209\)](https://doi.org/10.1061/(ASCE)0899-1561(2001)13:3(209)).
- [20] Mirmiran A, Shahawy M. Behavior of concrete columns confined by fiber composites. *J Struct Eng* 1997;123:583–90. [https://doi.org/10.1061/\(ASCE\)0733-9445\(1997\)123:5\(583\)](https://doi.org/10.1061/(ASCE)0733-9445(1997)123:5(583)).
- [21] Cao Y, Wu YF, Jiang C. Stress-strain relationship of FRP confined concrete columns under combined axial load and bending moment. *Compos Part B Eng* 2018;134:207–17. <https://doi.org/10.1016/j.compositesb.2017.09.063>.
- [22] Shan B, Gui FC, Monti G, Xiao Y. Effectiveness of CFRP confinement and compressive strength of square concrete columns. *J Compos Constr* 2019;23:04019043. [https://doi.org/10.1061/\(asce\)cc.1943-5614.0000967](https://doi.org/10.1061/(asce)cc.1943-5614.0000967).

- [23] Feng P, Cheng S, Bai Y, Ye L. Mechanical behavior of concrete-filled square steel tube with FRP-confined concrete core subjected to axial compression. *Compos Struct* 2015;123:312–24. <https://doi.org/10.1016/j.compstruct.2014.12.053>.
- [24] Teng JG, Yu T, Wong YL, Dong SL. Hybrid FRP–concrete–steel tubular columns: Concept and behavior. *Constr Build Mater* 2007;21:846–54. <https://doi.org/10.1016/j.conbuildmat.2006.06.017>.
- [25] Han DJ, Chen WF. A nonuniform hardening plasticity model for concrete materials. *Mech Mater* 1985;4:283–302. [https://doi.org/10.1016/0167-6636\(85\)90025-0](https://doi.org/10.1016/0167-6636(85)90025-0).
- [26] Lee J, Fenves GL. Plastic-damage model for cyclic loading of concrete structures. *J Eng Mech* 1998;124:892–900. [https://doi.org/10.1061/\(ASCE\)0733-9399\(1998\)124:8\(892\)](https://doi.org/10.1061/(ASCE)0733-9399(1998)124:8(892)).
- [27] Grassl P, Lundgren K, Gylltoft K. Concrete in compression: A plasticity theory with a novel hardening law. *Int J Solids Struct* 2002;39:5205–23. [https://doi.org/10.1016/S0020-7683\(02\)00408-0](https://doi.org/10.1016/S0020-7683(02)00408-0).
- [28] Papanikolaou VK, Kappos AJ. Confinement-sensitive plasticity constitutive model for concrete in triaxial compression. *Int J Solids Struct* 2007;44:7021–48. <https://doi.org/10.1016/j.ijsolstr.2007.03.022>.
- [29] Paliwal B, Hammi Y, Moser RD, Horstemeyer MF. A three-invariant cap-plasticity damage model for cementitious materials. *Int J Solids Struct* 2017;108:186–202. <https://doi.org/10.1016/j.ijsolstr.2016.12.015>.
- [30] Bao JQ, Long X, Tan KH, Lee CK. A new generalized Drucker-Prager flow rule for concrete under compression. *Eng Struct* 2013;56:2076–82. <https://doi.org/10.1016/j.engstruct.2013.08.025>.

- [31] Mirmiran A, Zagers K, Yuan W. Nonlinear finite element modeling of concrete confined by fiber composites. *Finite Elem Anal Des* 2000;35:79–96. [https://doi.org/10.1016/S0168-874X\(99\)00056-6](https://doi.org/10.1016/S0168-874X(99)00056-6).
- [32] Rousakis TC, Karabinis AI, Kioussis PD, Tefers R. Analytical modelling of plastic behaviour of uniformly FRP confined concrete members. *Compos Part B Eng* 2008;39:1104–13. <https://doi.org/10.1016/j.compositesb.2008.05.001>.
- [33] Karabinis AI, Rousakis TC. Concrete confined by FRP material: A plasticity approach. *Eng Struct* 2002;24:923–32. [https://doi.org/10.1016/S0141-0296\(02\)00011-1](https://doi.org/10.1016/S0141-0296(02)00011-1).
- [34] Yu T, Teng JG, Wong YL, Dong SL. Finite element modeling of confined concrete-I: Drucker-Prager type plasticity model. *Eng Struct* 2010;32:665–79. <https://doi.org/10.1016/j.engstruct.2009.11.014>.
- [35] Dassault Systemes. ABAQUS: Theory and User's manuals 2020.
- [36] Jiang JF, Wu YF. Identification of material parameters for Drucker-Prager plasticity model for FRP confined circular concrete columns. *Int J Solids Struct* 2012;49:445–56. <https://doi.org/10.1016/j.ijsolstr.2011.10.002>.
- [37] Mohammadi M, Dai JG, Wu YF, Bai YL. Development of extended Drucker–Prager model for non-uniform FRP-confined concrete based on triaxial tests. *Constr Build Mater* 2019;224:1–18. <https://doi.org/10.1016/j.conbuildmat.2019.07.061>.
- [38] Yu T, Teng JG, Wong YL, Dong SL. Finite element modeling of confined concrete-II: Plastic-damage model. *Eng Struct* 2010;32:680–91. <https://doi.org/10.1016/j.engstruct.2009.11.013>.

- [39] Mohammadi M, Wu YF. Modified plastic-damage model for passively confined concrete based on triaxial tests. *Compos Part B Eng* 2019;159:211–23. <https://doi.org/10.1016/j.compositesb.2018.09.074>.
- [40] Mohammadi M, Wu YF. Triaxial test for concrete under non-uniform passive confinement. *Constr Build Mater* 2017;138:455–68. <https://doi.org/10.1016/j.conbuildmat.2017.02.032>.
- [41] Hany NF, Hantouche EG, Harajli MH. Finite element modeling of FRP-confined concrete using modified concrete damaged plasticity. *Eng Struct* 2016;125:1–14. <https://doi.org/10.1016/j.engstruct.2016.06.047>.
- [42] Ribeiro F, Sena-Cruz J, Branco FG, Júlio E. 3D finite element model for hybrid FRP-confined concrete in compression using modified CDPM. *Eng Struct* 2019;190:459–79. <https://doi.org/10.1016/j.engstruct.2019.04.027>.
- [43] Bhartiya R, Sahoo DR, Verma A. Modified damaged plasticity and variable confinement modelling of rectangular CFT columns. *J Constr Steel Res* 2021;176. <https://doi.org/10.1016/j.jcsr.2020.106426>.
- [44] Carrazedo R, Mirmiran A, de Hanai JB. Plasticity based stress-strain model for concrete confinement. *Eng Struct* 2013;48:645–57. <https://doi.org/10.1016/j.engstruct.2012.12.014>.
- [45] Piscesa B, Attard MM, Samani AK. A lateral strain plasticity model for FRP confined concrete. *Compos Struct* 2016;158:160–74. <https://doi.org/10.1016/j.compstruct.2016.09.028>.
- [46] Farahmandpour C, Dartois S, Quiertant M, Berthaud Y, Dumontet H. A concrete damage–plasticity model for FRP confined columns. *Mater Struct Constr* 2017;50:14–20. <https://doi.org/10.1617/s11527-017-1016-8>.

- [47] Piscesa B, Attard MM, Samani AK, Tangaramvong S. Plasticity constitutive model for stress-strain relationship of confined concrete. *ACI Mater J* 2017;114:361–71. <https://doi.org/10.14359/51689428>.
- [48] Feng P, Meng X, Chen JF, Ye L. Mechanical properties of structures 3D printed with cementitious powders. *Constr Build Mater* 2015;93:486–97. <https://doi.org/10.1016/j.conbuildmat.2015.05.132>.
- [49] Feng P, Cheng S, Yu T. Seismic performance of hybrid columns of concrete-filled square steel tube with FRP-confined concrete core. *J Compos Constr* 2018;22:04018015. [https://doi.org/10.1061/\(ASCE\)CC.1943-5614.0000849](https://doi.org/10.1061/(ASCE)CC.1943-5614.0000849).
- [50] Ding FX, Fang C, Bai Y, Gong YZ. Mechanical performance of stirrup-confined concrete-filled steel tubular stub columns under axial loading. *J Constr Steel Res* 2014;98:146–57. <https://doi.org/10.1016/j.jcsr.2014.03.005>.
- [51] Teng JG, Wang JJ, Lin G, Zhang J, Feng P. Compressive behavior of concrete-filled steel tubular columns with internal high-strength steel spiral confinement. *Adv Struct Eng* 2021.
- [52] Lin G, Zeng JJ, Teng JG, Li LJ. Behavior of large-scale FRP-confined rectangular RC columns under eccentric compression. *Eng Struct* 2020;216. <https://doi.org/10.1016/j.engstruct.2020.110759>.
- [53] Yu T, Zhang S, Huang L, Chan C. Compressive behavior of hybrid double-skin tubular columns with a large rupture strain FRP tube. *Compos Struct* 2017;171:10–8. <https://doi.org/10.1016/j.compstruct.2017.03.013>.
- [54] Pietruszczak S, Jiang J, Mirza FA. An elastoplastic constitutive model for concrete. *Int J Solids Struct* 1988;24:705–22. [https://doi.org/10.1016/0020-7683\(88\)90018-2](https://doi.org/10.1016/0020-7683(88)90018-2).

- [55] Lubliner J, Oliver J, Oller S, Oñate E. A plastic-damage model for concrete. *Int J Solids Struct* 1989;25:299–326. [https://doi.org/10.1016/0020-7683\(89\)90050-4](https://doi.org/10.1016/0020-7683(89)90050-4).
- [56] Etse G, Willam K. Fracture energy formulation for inelastic behavior of plain concrete. *J Eng Mech* 1994;120:1983–2011. [https://doi.org/10.1061/\(ASCE\)0733-9399\(1994\)120:9\(1983\)](https://doi.org/10.1061/(ASCE)0733-9399(1994)120:9(1983)).
- [57] Piscesa B, Attard MM, Samani AK. 3D Finite element modeling of circular reinforced concrete columns confined with FRP using a plasticity based formulation. *Compos Struct* 2018;194:478–93. <https://doi.org/10.1016/j.compstruct.2018.04.039>.
- [58] Červenka J, Papanikolaou VK. Three dimensional combined fracture-plastic material model for concrete. *Int J Plast* 2008;24:2192–220. <https://doi.org/10.1016/j.ijplas.2008.01.004>.
- [59] Grassl P, Jirásek M. Damage-plastic model for concrete failure. *Int J Solids Struct* 2006;43:7166–96. <https://doi.org/10.1016/j.ijsolstr.2006.06.032>.
- [60] Imran I, Pantazopoulou SJ. Plasticity model for concrete under triaxial compression. *J Eng Mech* 2001;127:281–90. [https://doi.org/10.1061/\(ASCE\)0733-9399\(2001\)127:3\(281\)](https://doi.org/10.1061/(ASCE)0733-9399(2001)127:3(281)).
- [61] Drucker DC, Prager W. Soil mechanics and plastic analysis or limit design. *Q Appl Math* 1952;10:157–65. <https://doi.org/10.1090/qam/48291>.
- [62] Rudnicki JW, Rice JR. Conditions for the localization of deformation in pressure-sensitive dilatant materials. *J Mech Phys Solids* 1975;23:371–94. [https://doi.org/10.1016/0022-5096\(75\)90001-0](https://doi.org/10.1016/0022-5096(75)90001-0).
- [63] Bazant ZP. Endochronic inelasticity and incremental plasticity. *Int J Solids Struct* 1978;14:691–714. [https://doi.org/10.1016/0020-7683\(78\)90029-X](https://doi.org/10.1016/0020-7683(78)90029-X).
- [64] Tastani SPP, Balafas I, Dervisis A, Pantazopoulou SJJ. Effect of core compaction on deformation capacity of FRP-jacketed concrete columns. *Constr Build Mater* 2013;47:1078–92. <https://doi.org/10.1016/j.conbuildmat.2013.05.092>.

- [65] Smith SS, William KJ, Gerstle KH, Sture S. Concrete over the top, or: Is there life after peak? *ACI Mater J* 1989;86:491–7.
- [66] Valanis KC, Lee CF. Some recent developments of the endochronic theory with applications. *Nucl Eng Des* 1982;69:327–44. [https://doi.org/10.1016/0029-5493\(82\)90181-9](https://doi.org/10.1016/0029-5493(82)90181-9).
- [67] Wriggers P, Moftah SO. Mesoscale models for concrete: Homogenisation and damage behaviour. *Finite Elem Anal Des* 2006;42:623–36. <https://doi.org/10.1016/j.finel.2005.11.008>.
- [68] Unger JF, Eckardt S. Multiscale modeling of concrete. *Arch Comput Methods Eng* 2011;18:341–93. <https://doi.org/10.1007/s11831-011-9063-8>.
- [69] Samani AK, Attard MM. Lateral strain model for concrete under compression. *ACI Struct J* 2014;111:441–51. <https://doi.org/10.14359/51686532>.
- [70] Lim JC, Ozbakkaloglu T. Unified stress-strain model for FRP and actively confined normal-strength and high-strength concrete. *J Compos Constr* 2015;19:04014072. [https://doi.org/10.1061/\(ASCE\)CC.1943-5614.0000536](https://doi.org/10.1061/(ASCE)CC.1943-5614.0000536).
- [71] Li B, Jiang J, Xiong H, Zhan Y, Wu Z, Cunningham LS. Improved concrete plastic-damage model for FRP-confined concrete based on true tri-axial experiment. *Compos Struct* 2021;269:114051. <https://doi.org/10.1016/j.compstruct.2021.114051>.
- [72] Grassl P, Xenos D, Nyström U, Rempling R, Gylltoft K. CDPM2: A damage-plasticity approach to modelling the failure of concrete. *Int J Solids Struct* 2013;50:3805–16. <https://doi.org/10.1016/j.ijsolstr.2013.07.008>.
- [73] Ozbakkaloglu T, Gholampour A, Lim JC. Damage-plasticity model for FRP-confined normal-strength and high-strength concrete. *J Compos Constr* 2016;20:04016053. [https://doi.org/10.1061/\(asce\)cc.1943-5614.0000712](https://doi.org/10.1061/(asce)cc.1943-5614.0000712).

- [74] Wight JK, MacGregor JG. Reinforced concrete mechanics & design. 6th ed. Pearson; 2012.
- [75] Hussein A, Marzouk H. Behavior of high-strength concrete under biaxial stresses. *ACI Struct J* 2000;97:27–36. <https://doi.org/10.14359/802>.
- [76] Ottosen NS. Constitutive model for short-time loading of concrete. *J Eng Mech Div* 1979;105:127–41.
- [77] Soleymani HR. Structural design properties of concrete for a bridge in Alberta. *Can J Civ Eng* 2006;33:199–205. <https://doi.org/10.1139/105-092>.
- [78] Lu X, Hsu CTT. Tangent Poisson's ratio of high-strength concrete in triaxial compression. *Mag Concr Res* 2007;59:69–77. <https://doi.org/10.1680/macr.2007.59.1.69>.
- [79] Tasdemir MA, Tasdemir C, Akyüz S, Jefferson AD, Lydon FD, Barr BIG. Evaluation of strains at peak stresses in concrete: A three-phase composite model approach. *Cem Concr Compos* 1998;20:301–18. [https://doi.org/10.1016/S0958-9465\(98\)00012-2](https://doi.org/10.1016/S0958-9465(98)00012-2).
- [80] Popovics S. A numerical approach to the complete stress-strain curve of concrete. *Cem Concr Res* 1973;3:583–99. [https://doi.org/10.1016/0008-8846\(73\)90096-3](https://doi.org/10.1016/0008-8846(73)90096-3).
- [81] Yang KH, Mun JH, Cho MS, Kang THK. Stress-strain model for various unconfined concretes in compression. *ACI Mater J* 2014;111. <https://doi.org/10.14359/51686631>.
- [82] Samani AK, Attard MM. A stress-strain model for uniaxial and confined concrete under compression. *Eng Struct* 2012;41:335–49. <https://doi.org/10.1016/j.engstruct.2012.03.027>.
- [83] Binici B. An analytical model for stress-strain behavior of confined concrete. *Eng Struct* 2005;27:1040–51. <https://doi.org/10.1016/j.engstruct.2005.03.002>.
- [84] ACI Committee 318. Building Code Requirements for Structural Concrete. 2014. <https://doi.org/10.14359/51716937>.

- [85] Lahlou K, Aïtecin PC, Chaallal O. Behaviour of high-strength concrete under confined stresses. *Cem Concr Compos* 1992;14:185–93. [https://doi.org/10.1016/0958-9465\(92\)90012-K](https://doi.org/10.1016/0958-9465(92)90012-K).
- [86] Lu X, Hsu CTT. Stress-strain relations of high-strength concrete under triaxial compression. *J Mater Civ Eng* 2007;19:261–8. [https://doi.org/10.1061/\(ASCE\)0899-1561\(2007\)19:3\(261\)](https://doi.org/10.1061/(ASCE)0899-1561(2007)19:3(261)).
- [87] Sfer D, Carol I, Gettu R, Etse G. Study of the behavior of concrete under triaxial compression. *J Eng Mech* 2002;128:156–63. [https://doi.org/10.1061/\(ASCE\)0733-9399\(2002\)128:2\(156\)](https://doi.org/10.1061/(ASCE)0733-9399(2002)128:2(156)).
- [88] Zhang M, Liu X, Wang Y, Wang X. Parameter distribution characteristics of material fatigue life using improved bootstrap method. *Int J Damage Mech* 2019;28:772–93. <https://doi.org/10.1177/1056789518792658>.
- [89] Henderson AR. The bootstrap: A technique for data-driven statistics. Using computer-intensive analyses to explore experimental data. *Clin Chim Acta* 2005;359:1–26. <https://doi.org/10.1016/j.cccn.2005.04.002>.
- [90] Lim JC, Ozbakkaloglu T. Lateral Strain-to-axial strain relationship of confined concrete. *J Struct Eng* 2014;141:04014141. [https://doi.org/10.1061/\(asce\)st.1943-541x.0001094](https://doi.org/10.1061/(asce)st.1943-541x.0001094).
- [91] Červenka V, Jendele L, Červenka J. ATENA program documentation part 1: Theory. *Atena* 2012:1–282.
- [92] Abu Al-Rub RK, Kim SMM. Computational applications of a coupled plasticity-damage constitutive model for simulating plain concrete fracture. *Eng Fract Mech* 2010;77:1577–603. <https://doi.org/10.1016/j.engfracmech.2010.04.007>.
- [93] Patzák B, Bittnar Z. Design of object oriented finite element code. *Adv Eng Softw* 2001;32:759–67. [https://doi.org/10.1016/S0965-9978\(01\)00027-8](https://doi.org/10.1016/S0965-9978(01)00027-8).

- [94] Simo JC, Taylor RL. Consistent tangent operators for rate-independent elastoplasticity. *Comput Methods Appl Mech Eng* 1985;48:101–18. [https://doi.org/10.1016/0045-7825\(85\)90070-2](https://doi.org/10.1016/0045-7825(85)90070-2).
- [95] Gu Q, Conte JP, Yang Z, Elgamal A. Consistent tangent moduli for multi-yield-surface J2 plasticity model. *Comput Mech* 2011;48:97–120. <https://doi.org/10.1007/s00466-011-0576-7>.
- [96] Jiang J, Xiao P, Li B. True-triaxial compressive behaviour of concrete under passive confinement. *Constr Build Mater* 2017;156:584–98. <https://doi.org/10.1016/j.conbuildmat.2017.08.143>.
- [97] ASTM International. Standard test method for static modulus of elasticity and Poisson's ratio of concrete in compression. 2014. https://doi.org/10.1520/C0469_C0469M-14E01.
- [98] Jirásek M, Rolshoven S. Comparison of integral-type nonlocal plasticity models for strain-softening materials. *Int J Eng Sci* 2003;41:1553–602. [https://doi.org/10.1016/S0020-7225\(03\)00027-2](https://doi.org/10.1016/S0020-7225(03)00027-2).
- [99] Rub RKA Al, Darabi MK, Masad EA. A straightforward numerical technique for finite element implementation of non-local gradient-dependent continuum damage mechanics theories. *Int J Theor Appl Multiscale Mech* 2010;1:352. <https://doi.org/10.1504/ijtamm.2010.038281>.
- [100] Kenawy M, Kunnath S, Kolwankar S, Kanvinde A. Fiber-based nonlocal formulation for simulating softening in reinforced concrete beam-columns. *J Struct Eng* 2018;144. [https://doi.org/10.1061/\(ASCE\)ST.1943-541X.0002218](https://doi.org/10.1061/(ASCE)ST.1943-541X.0002218).

Appendix A Relationship between the Haigh–Westergaard coordinates and the principal stresses

The first principal invariant of stress tensor $\{I_1(\boldsymbol{\sigma})\}$, and the second and third principal invariants of the deviatoric stress tensor $\{J_2(\boldsymbol{\sigma}), J_3(\boldsymbol{\sigma})\}$ are related to the principal stresses ($\sigma_1 > \sigma_2 > \sigma_3$) as follows:

$$\begin{cases} I_1(\boldsymbol{\sigma}) = \sigma_1 + \sigma_2 + \sigma_3 \\ J_2(\boldsymbol{\sigma}) = \frac{1}{6}[(\sigma_1 - \sigma_2)^2 + (\sigma_2 - \sigma_3)^2 + (\sigma_3 - \sigma_1)^2] \\ J_3(\boldsymbol{\sigma}) = (\sigma_1 - I_1)(\sigma_2 - I_1)(\sigma_3 - I_1) \end{cases} \quad (\text{A1})$$

and the Haigh-Westergaard coordinates are expressed as follows:

$$\xi = \frac{I_1(\boldsymbol{\sigma})}{\sqrt{3}}, \rho = \sqrt{2J_2(\boldsymbol{\sigma})}, \cos 3\theta = \frac{3\sqrt{3}J_3(\boldsymbol{\sigma})}{2J_2(\boldsymbol{\sigma})^{3/2}} \quad (\text{A2})$$

The principal stresses can be obtained from the Haigh-Westergaard coordinates as follows:

$$\begin{bmatrix} \sigma_1 \\ \sigma_2 \\ \sigma_3 \end{bmatrix} = \frac{1}{\sqrt{3}} \begin{bmatrix} \xi \\ \xi \\ \xi \end{bmatrix} + \sqrt{\frac{2}{3}} \rho \begin{bmatrix} \cos \theta \\ \cos \left(\theta - \frac{2\pi}{3} \right) \\ \cos \left(\theta + \frac{2\pi}{3} \right) \end{bmatrix} \quad (\text{A3})$$

Appendix B Effect of potential-surface deviatoric trace on plastic strain increment direction

In Fig. B.1a, the values of ϑ for the three types of traces are shown for $0^\circ \leq \theta \leq 60^\circ$. For the non-circular traces, the value of $0.55 \leq \rho \leq 0.75$ is used. For all three traces, $\vartheta = \theta$ at $\theta = 0^\circ$ and 60° . The circular trace yields $\vartheta = \theta$ at all intermediate values, while for the non-circular traces, $\vartheta < \theta$. The ϑ of the trefoil trace decreases faster than that of the circular trace but becomes negative when θ is relatively small, which is caused by the concavity of the trace.

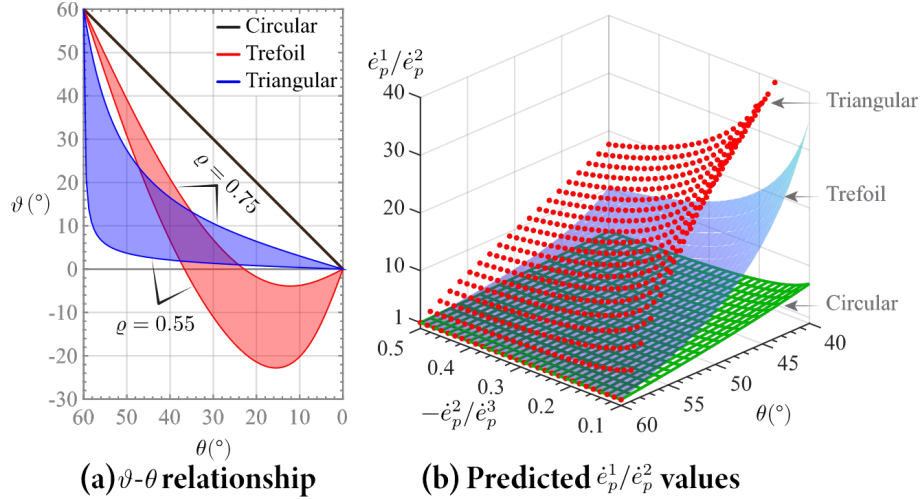


Fig. B.1 Effect of potential-surface deviatoric trace on plastic deformation non-uniformity

It has also been well-established that the potential surface needs to be convex to satisfy the thermodynamic dissipation inequality, which means that the potential surface may become thermodynamically problematic if it becomes concave (e.g., see the discussions given by Grassl and Jirásek [59]). The ϑ of the bulged triangular trace decreases even faster once $\theta < 60^\circ$, and then gradually approaches zero. This behavior is preferred numerically, and the rate of initial decrease of ϑ can be tuned by the value of ρ . The relationships among the three plastic strain components, assuming $\dot{\epsilon}_1^p > \dot{\epsilon}_2^p > 0 > \dot{\epsilon}_3^p$ for compression-dominant stress conditions, are prescribed by the following equation:

$$\frac{\dot{\epsilon}_1^p - \dot{\epsilon}_2^p}{\dot{\epsilon}_2^p - \dot{\epsilon}_3^p} = \frac{\sin(60^\circ - \vartheta)}{\sin(\vartheta)} \quad (\text{B1})$$

The corresponding values of $\dot{\epsilon}_1^p/\dot{\epsilon}_2^p$ predicted by the three traces are shown in Fig. B.1b for $\rho = 0.65$. It is seen that the bulged triangular trace gives the largest difference between $\dot{\epsilon}_1^p$ and $\dot{\epsilon}_2^p$ due to the smallest ϑ .

Appendix C Definition of volumetric parameters

Fig. C.1 schematically shows the definitions of the three parameters, β , α , and ψ , on the stress-field, strain-field, and 2D axial-lateral strain-field, respectively. In the stress-field (Fig. C.1a) on the Rendulic plane, the angle between the normal of the potential surface and the ρ axis is defined as the potential angle β , and hence $\tan \beta$ is the potential parameter. Positive and negative values of β indicate respectively plastic volumetric dilation and compaction. In the strain-space (Fig. C.1b) on the Rendulic plane, the angle of the plastic strain increment with the ρ axis is defined as the dilation angle α , and hence $\tan \alpha$ is the dilation rate.

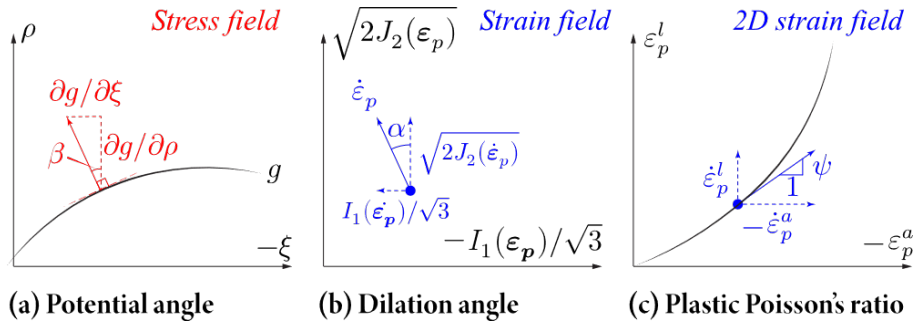


Fig. C.1 Illustration of volumetric parameters

The use of Haigh–Westergaard coordinates for both the stress $\{\xi(\boldsymbol{\sigma}), \rho(\boldsymbol{\sigma})\}$ and the strain spaces $\{\xi(\boldsymbol{\epsilon}_p), \rho(\boldsymbol{\epsilon}_p)\}$ [28,29] yields the straightforward relationship: $\tan \beta = \tan \alpha$ as follows. For the Haigh–Westergaard coordinates, it has:

$$\tan \beta = \frac{\partial g / \partial \xi}{\partial g / \partial \rho}, \tan \alpha = \frac{I_1(\dot{\boldsymbol{\epsilon}}_p) / \sqrt{3}}{\sqrt{2J_2(\dot{\boldsymbol{\epsilon}}_p)}} \quad (\text{C1})$$

The flow rule gives: $\dot{\varepsilon}_p^1 = \dot{\lambda} g_{\sigma_1} = \dot{\lambda} \left(\frac{\partial g}{\partial \xi} \frac{\partial \xi}{\partial \sigma_1} + \frac{\partial g}{\partial \rho} \frac{\partial \rho}{\partial \sigma_1} \right)$, where $\frac{\partial \xi}{\partial \sigma_1} = \frac{\sqrt{3}}{3}$ and $\frac{\partial \rho}{\partial \sigma_1} = \frac{2\sigma_1 - \sigma_2 - \sigma_3}{3\sqrt{2}\sqrt{J_2}}$.

Therefore, it can be readily obtained from algebra:

$$\dot{\varepsilon}_p^1 + \dot{\varepsilon}_p^2 + \dot{\varepsilon}_p^3 = \sqrt{3}\dot{\lambda} \partial g / \partial \xi \quad (\text{C2})$$

and

$$\sqrt{(\dot{\varepsilon}_p^1 - \dot{\varepsilon}_p^2)^2 + (\dot{\varepsilon}_p^2 - \dot{\varepsilon}_p^3)^2 + (\dot{\varepsilon}_p^3 - \dot{\varepsilon}_p^1)^2} = \sqrt{3}\dot{\lambda} \partial g / \partial \rho \quad (\text{C3})$$

as a result, it yields

$$\tan \alpha = \frac{(\dot{\varepsilon}_1 + \dot{\varepsilon}_2 + \dot{\varepsilon}_3) / \sqrt{3}}{\sqrt{\frac{2}{6} \sqrt{(\dot{\varepsilon}_1 - \dot{\varepsilon}_2)^2 + (\dot{\varepsilon}_2 - \dot{\varepsilon}_3)^2 + (\dot{\varepsilon}_3 - \dot{\varepsilon}_1)^2}}} = \tan \beta \quad (\text{C4})$$

In some other studies such as Karabinis and Rousakis [33] and Yu et al. [34], the stress space

coordinates are $\{I_1(\boldsymbol{\sigma}), \sqrt{J_2(\boldsymbol{\sigma})}\}$, and the strain space coordinates are $\{I_1(\boldsymbol{\varepsilon}_p), \sqrt{J_2(\boldsymbol{\varepsilon}_p)}\}$.

Following from the same process, it yields: $\tan \alpha = 6 \tan \beta$. In yet other studies (e.g., [36]), the

stress space is described by $\{\xi(\boldsymbol{\sigma}), \sqrt{J_2(\boldsymbol{\sigma})}\}$ and the strain space by $\{I_1(\boldsymbol{\varepsilon}_p), \sqrt{J_2(\boldsymbol{\varepsilon}_p)}\}$.

Accordingly, it yields: $\sqrt{3}\tan \alpha = 2 \tan \beta$. Moreover, the dilation rate is defined as the ratio between the total lateral and axial strain increments in Lim and Ozbakkaloglu [17] and Piscosa et al. [45].

Considering only the plastic volumetric behavior, the 3D strain-space can be reduced into a 2D field of lateral ($\dot{\varepsilon}_p^l = 1/2(\dot{\varepsilon}_p^1 + \dot{\varepsilon}_p^2)$) and axial ($\dot{\varepsilon}_p^a = \dot{\varepsilon}_p^3$) strains. Fig. C.1c shows the 2D plastic strain field, where the slope of the strain curve is defined as the plastic Poisson's ratio $\psi = -\dot{\varepsilon}_p^l / \dot{\varepsilon}_p^a$. The relationship between ψ and α is readily obtained from the above equations as:

$$\tan \alpha = \frac{2\psi - 1}{\sqrt{2}(1 + \psi)} \quad (\text{C5})$$

or

$$\psi = \frac{1+\sqrt{2}\tan\alpha}{2-\sqrt{2}\tan\alpha} \quad (\text{C6})$$

Appendix D Plastic volumetric evolution in pre-transition regime

The values of A_0 and A_k are determined as follows. At the initial state, $h = h_0$, so $\boldsymbol{\sigma} = [0\ 0\ -\sigma_0\ 0\ 0\ 0]^T$; at the transition state, $h = 1$, so $\boldsymbol{\sigma} = [0\ 0\ -f_c\ 0\ 0\ 0]^T$. Considering only the volumetric behavior, the potential function is:

$$g(\xi, \rho) = \rho + A \cdot (B_0 \cdot f_c - \xi) \cdot \ln \frac{B_0 \cdot f_c - \xi}{\xi_0} = 0 \quad (\text{D1})$$

and by definition:

$$\psi = -\frac{\partial g}{\partial \sigma_x} / \frac{\partial g}{\partial \sigma_z} \quad (\text{D2})$$

at $h = h_0$, the following results from Eq.(D1):

$$\xi_0 = e^{\left\{ \frac{\sqrt{6}\sigma_0}{A_0(3B_0f_c + \sqrt{3}\sigma_0)} \right\}} (B_0f_c + \sigma_0/\sqrt{3}) \quad (\text{D3})$$

hence

$$A_0 = \frac{3\sqrt{2}\sigma_0 + \sqrt{6}B_0f_c - 2\sqrt{6}B_0f_c\psi_0}{2(\psi_0 + 1)(\sqrt{3}B_0f_c + \sigma_0)} \quad (\text{D4})$$

The value of $\sigma_0 = (f_c^{1.855})/60$ suggested by Papanikolaou and Kappos [28] can be used to compute A_0 . At $h = 1$, Eq.(D1) yields:

$$\xi_0 = f_c e^{\left\{ \frac{\sqrt{6}}{A_k(3B_0 + \sqrt{3})} \right\}} (B_0 + 1/\sqrt{3}) \quad (\text{D5})$$

hence

$$A_k = \frac{3\sqrt{2} + \sqrt{6}B_0 - 2\sqrt{6}B_0\psi_k}{2(\psi_k + 1)(\sqrt{3}B_0 + 1)} \quad (\text{D6})$$

Appendix E Relationship between ductility measure and confinement

The relationship between χ_p and η is established based on the experimentally obtained relationship between $\varepsilon^{k,*}/\varepsilon^k$ and σ_l . The stress state at the transition state under uniform confinement is $\boldsymbol{\sigma} = [\sigma_l \ \sigma_l \ \sigma_3 \ 0 \ 0 \ 0]^T$, which dwells on the failure surface. Therefore, substituting this stress state to the failure surface yields:

$$\sigma_3 = \sigma_l - \sqrt{f_c^2 - \frac{3e\sigma_l(f_c^2 - f_t^2)}{f_t(1+e)}} \quad (\text{E1})$$

then with $\xi = (2\sigma_l + \sigma_3)/\sqrt{3}$, $\eta = (-\xi/\sqrt{3} - f_c/3)/f_c$ ($r(\theta) = 1$ is omitted for clarity) is rewritten as:

$$\eta = \frac{-\sigma_l}{f_c} - \frac{1}{3} + \sqrt{\frac{1}{9} - \frac{e\sigma_l(\sigma_l^2 - f_t^2)}{3f_c^2 f_t(e+1)}} \quad (\text{E2})$$

Further, to express $\varepsilon^{k,*}/\varepsilon^k$ with χ_p , the total strain is decomposed into elastic and plastic strains as:

$$\varepsilon^{k,*} = \chi_p \varepsilon_p^k + \varepsilon_e^{k,*} \quad (\text{E3})$$

where $\varepsilon_p^k = \varepsilon^k - \varepsilon_e^k$, $\varepsilon_e^k = -f_c/E$, and $\varepsilon_e^{k,*} = \sigma_3/E$. If a reasonable value (e.g., $K = 18$) is used (see Eq. (23)), the following relationship is thus obtained:

$$\frac{\chi_p \varepsilon_p^k + \varepsilon_e^{k,*}}{\varepsilon_p^k + \varepsilon_e^k} = 1 - 18 \frac{\sigma_l}{f_c} \quad (\text{E4})$$

By substituting ε_p^k , ε_e^k , and σ_l into the above equation, an implicit relationship between χ_p and η is obtained. A polynomial expression that is mathematically much simpler than the implicit relationship was numerically established as follows:

$$\chi_p = 1 + (26.3 + 0.437f_c - 0.00075f_c^2)\eta - (18.8 + 0.0975f_c)\eta^2 + 8\eta^3 \quad (\text{E5})$$

The values of χ_p calculated from Eq. (E5) and those from the implicit relationship are compared in Fig. E.1 for f_c values ranging from 20 to 140 MPa and η values ranging from 0 to 2, which validates the accuracy of Eq. (E5).

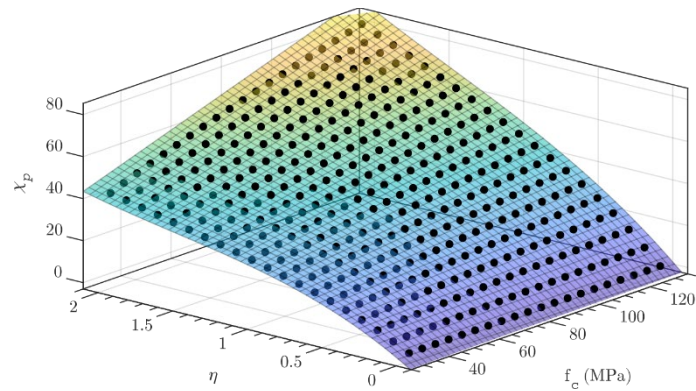


Fig. E.1 Calibration of the ductility measure